Coupling compositional gas liquid Darcy and free gas flows at porous and free flow domains interface

Roland Masson, L Trenty, Yumeng Zhang

Coupling compositional gas liquid Darcy and free gas flows at porous and free flow domains interface

R. Masson*, L. Trenty†, Y. Zhang‡

December 5, 2015

Abstract

This paper proposes an efficient splitting algorithm to solve coupled gas liquid Darcy and free gas flows at the interface between a porous medium and a free flow domains. A reduced model using a 1D approximation of the gas free flow is also introduced. This reduced model uses an approximation of the gas molar fraction boundary layer thickness in the free flow domain based on a low frequency approximation of a Steklov Poincaré type operator. The splitting algorithm and the reduced model are applied in particular to the modelling of the mass exchanges at the interface between the storage and the ventilation galleries in radioactive waste deposits.

1 Introduction

Flow and transport processes in domains composed of a porous medium and an adjacent free-flow region appear in a wide range of applications. It includes for example, in industrial drying applications, the production of building materials, food processing, and wood and paper production, or also, in environmental applications, land-atmospheric interaction and soil evaporation and evapotranspiration. In this article we will focus on the design of efficient algorithms to simulate the mass exchanges at the interface between the porous and free flow regions, assuming a fixed temperature in the porous and free flow domains. The effect of the vaporization on the temperature is neglected and will be considered in a future work. Typically in drying processes, the porous medium initially saturated with the liquid phase is dried by suction in the neighbourhood of the interface between the porous and free flow domains. The gas phase penetrates in the porous domain and the liquid phase is vaporized in the free flow domain. In this work, our focus is not only on the drying of the porous medium but also on the evolution of the gas composition in the free flow region. This is motivated by our main interest for such models to the prediction of the mass exchanges occurring at the interface between the radioactive waste deep geological repositories and the ventilation excavated galleries. In this application, the ventilation galleries must be proved to remain safe during the entire period of reversibility of the storage fixed to 100 years in France by the national savety authorities.

To model such physical processes, one needs to account in the porous medium for the flow of the liquid and gas phases including the vaporization of the water component in the gas phase and the dissolution of the gaseous components in the liquid phase. In the free flow region, a single phase gas free flow is considered assuming that the liquid phase is instantaneously vaporized at the interface.

*Laboratoire de Mathématiques J.A. Dieudonné, UMR 7351 CNRS, University Nice Sophia Antipolis, and team COFFEE, INRIA Sophia Antipolis Méditerranée, Parc Valrose 06108 Nice Cedex 02, France, roland.masson@unice.fr

†Andra, 1-7 rue Jean Monnet 92290 Chatenay-Malabry, France, laurent.trenty@andra.fr

‡Laboratoire de Mathématiques J.A. Dieudonné, UMR 7351 CNRS, University Nice Sophia Antipolis, and team COFFEE, INRIA Sophia Antipolis Méditerranée, Parc Valrose 06108 Nice Cedex 02, France, yumeng.zhang@unice.fr

This gas free flow has to be compositional to account for the change of the relative humidity in the free flow region which has a strong feedback on the liquid flow rate at the interface.

If many works have been performed to model and discretize the coupling of single phase Darcy and free flows (see the review [14]), there are much fewer works on the coupling of a two phase gas liquid compositional Darcy flow with a single phase compositional gas free flow. Such a coupled model has been recently proposed in [23, 3] using matching conditions at the interface between the porous medium and the free flow regions. These coupling conditions state the continuity of the molar normal flux of each component taking into account the instantaneous vaporization of the liquid phase, the continuity of the gas molar fractions, and the liquid gas thermodynamical equilibrium. In our case, the Beavers Joseph law [4] used in [23, 3] is replaced by a no slip condition due to the low permeability of the porous medium and we can also neglect in practice the gas pressure jump at the interface due to the weak normal gas velocity at the interface.

The main objective of this article is to design an efficient algorithm to solve this coupled problem. Sequential algorithms based on Dirichlet Neumann boundary conditions at the interface (see [12, 10] and the review [11]) are frequently used for solving drying problems. As mentioned in [12, 10], the stability of sequential algorithms requires very small time steps at the scale of the free flow leading to very large CPU times. In order to obtain an efficient algorithm, one needs to be able to use time steps at the scale of the porous medium with a quasi stationary computation of the free flow at each time step. For this purpose, fully coupled algorithms such as the ones developed in [3, 17, 22] have been introduced, but they lead to non linear and linear systems which are difficult and expensive to solve since they do not take advantage of the different levels of coupling in the non linear system.

This article develops a more efficient approach based on a splitting between the strongly and weakly coupled equations and unknowns of the full system. This approach can be used either as a fixed point algorithm leading to the fully coupled solution at convergence or simply as a sequential algorithm which will be shown to provide a sufficient accuracy compared with the fully coupled solution. Our choice of the splitting of the full system is based on the physical understanding of the strong and weak couplings in the system. On the one hand, the water molar fraction in the free flow region is strongly coupled to the liquid pressure and liquid flux at the porous and free flow domains interface due to the liquid gas thermodynamical equilibrium. On the other hand, the gas velocity perturbation in the free flow domain, which is induced by the coupling with the porous medium, is small compared with the forced convection velocity. Consequently, it has a weak feedback on the porous medium. Therefore, the idea of our splitting strategy is to solve, in a first step, the porous medium equations coupled to the convection diffusion equations for the gas molar fractions in the free flow domain at fixed velocity and pressure in the free flow domain. Then, the total molar normal flux at the interface is computed and used in the second step of the algorithm to compute the velocity and pressure in the free flow domain solving the Navier Stokes equations.

The second objective of this paper is to propose a reduced model taking into account the large longitudinal dimension of the ventilation galleries compared with their diameter allowing to reduce the model in the gallery to a 1D free flow. In the spirit of Convective Mass Transfer Coefficients CMTCs (see the review [11] and the references there in for a discussion about CMTCs). the model includes on the free flow side a gas molar fraction at the interface and a normal diffusion flux between the interface and the free flow domain modelling the gas molar fraction boundary layer. This normal diffusion flux involves the gas molar fraction boundary layer thickness as parameter which plays an essential role on the liquid evaporation rate at the interface. In our reduced model, this parameter is computed based on a low frequency approximation of a Steklov Poincaré type operator for the stationary convection diffusion equation at fixed velocity. It leads to a boundary layer thickness depending on the longitudinal coordinate x along the free flow domain.

In order to assess the efficiency of the splitting algorithm and the accuracy of the reduced model, a simple 2D setting exhibited in Figure 1 is used. In the porous medium Ω^p, we consider a compositional liquid gas Darcy flow using the phase pressures and component fugacities formulation introduced in [21]. In the free flow domain Ω^g, the turbulent nature of the flow is taken into account using an algebraic model leading to the computation of a turbulent profile. This longitudinal turbulent profile is a stationary solution of the RANS model (Reynolds Averaged Navier Stokes, see e.g. [7, 5]) without the coupling with the porous medium flow. Then, this turbulent profile $\mathbf{u}_t$ provides the turbulent dynamic viscosity μ_t and the turbulent diffusion D_t that are used to compute the velocity, pressure and gas molar fraction in Ω^g solving the RANS compositional model at fixed turbulent viscosity μ_t and diffusion D_t. The turbulent viscosity and diffusion can be fixed thanks to the small perturbation of the velocity and pressure induced by the coupling in the free flow region. Note also that the turbulent diffusion D_t plays an essential role in the liquid evaporation rate at the interface.

The 2D domain is discretized using a Cartesian mesh conforming at the interface and refined on both sides of the interface Γ in order to take into account the laminar boundary layer on the gallery side and the strong liquid pressure gradient on the porous medium side. The space discretization uses a Marker-And-Cell (MAC) scheme for the RANS model [16] and a cell centered finite volume scheme for the Darcy flow in Ω^p and for the convection diffusion equations in Ω^g. In both cases, the diffusive fluxes (Darcy and turbulent diffusion terms) are approximated by a two point flux and the convective numerical fluxes are obtained by a first order upwind scheme. The time integration uses an implicit Euler scheme.

Three test cases are considered. The first two test cases correspond to a data set given by Andra with a very low permeable porous medium for the geological storage of radioactive wastes and with either an horizontal or a vertical gallery. The third test case considers the convective drying of a porous medium with a much larger permeability of say 1 Darcy.

The outline of the paper is the following. In Section 2, the formulation of the coupled model is introduced using the phase pressures and component fugacities formulation in the porous medium. Then, the splitting algorithm is described. In Section 3 the reduced model using a 1D model in the free flow domain is described as well as the computation of the gas molar fraction boundary layer thickness. In Section 4, the 2D setting for our numerical experiments is detailed as well as the discretization in the porous medium and in the gallery. Then, the results of the three test cases are presented and discussed.

2 Formulation of the coupled model and splitting algorithm

Let Ω^p denote the porous medium domain and Ω^g the free flow domain. The interface between the two domains is denoted by $\Gamma = \partial\Omega^p \cap \partial\Omega^g$.

2.1 Formulation of the coupled model

Let $\alpha = g, l$ denote the gas and liquid phases assumed to be both defined by a mixture of components $i \in \mathcal{C}$ among which the water component denoted by e which can vaporize in the gas phase, and a set of gaseous components $j \in \mathcal{C} \setminus \{e\}$ which can dissolve in the liquid phase. The model is assumed to be isothermal with a fixed temperature T_e. Following [21], the gas liquid Darcy flow formulation uses the gas pressure p^g, the liquid pressure p^l, and the component fugacities $f = (f_i)_{i\in\mathcal{C}}$ as primary unknowns, denoted by $\mathcal{U} = (p^g, p^l, f)$ in the following. In this formulation, following [19], the component molar fractions $c^\alpha = (c_i^\alpha)_{i\in\mathcal{C}}$ of each phase $\alpha = g, l$ are the functions $c_i^\alpha(\mathcal{U})$ of $\mathcal{U}$ defined by inversion of the equations $f_i^\alpha(c^\alpha, p^g, p^l) = f_i$, $i \in \mathcal{C}$, where f_i^α is the fugacity of the

component i in the phase α. In addition, for $\alpha = g, l$, the phase pressure p^α is extended in the absence of the phase in such a way that the closure law $\sum_{i\in\mathcal{C}} c_i^\alpha(\mathcal{U}) = 1$ is always imposed (see [21]). The phase molar and mass densities, as well as the phase viscosities are denoted in the following by respectively $\zeta^\alpha(p^\alpha, c^\alpha)$, $\rho^\alpha(p^\alpha, c^\alpha)$, $\mu^\alpha(p^\alpha, c^\alpha)$ for $\alpha = g, l$. For the sake of simplicity, for $\xi = \zeta^\alpha$, ρ^α, or μ^α, we will still use the notation $\xi(\mathcal{U})$ for the function $\xi(p^\alpha, c^\alpha(\mathcal{U}))$.
Finally, we define the liquid saturation as the function $\mathcal{S}^l(\mathbf{x}, p^g - p^l)$ of $p_c = p^g - p^l$ defined by the inverse of the monotone graph extension of the capillary pressure function $p_c(\mathbf{x}, .)$, and we set $\mathcal{S}^g(\mathbf{x}, .) = 1 - \mathcal{S}^l(\mathbf{x}, .)$. This leads to the following set of equations for the unknowns $\mathcal{U}$ in the porous medium

$$\begin{cases} \phi\partial_t n_i(\mathbf{x},\mathcal{U}) + \mathrm{div}\Big(\sum_{\alpha=g,l} m_i^\alpha(\mathbf{x},\mathcal{U})\mathbf{K}\Big(\nabla p^\alpha - \rho^\alpha(\mathcal{U})\mathbf{g}\Big)\Big) = 0,\ i\in\mathcal{C} & \text{on } \Omega^p\times(0,T), \\ \sum_{i\in\mathcal{C}} c_i^\alpha(\mathcal{U}) = 1,\ \alpha = g, l & \text{on } \Omega^p\times(0,T), \end{cases} \tag{1}$$

with the number of mole of the component i per unit pore volume defined by

$$n_i(\mathbf{x},\mathcal{U}) = \sum_{\alpha=l,g} c_i^\alpha(\mathcal{U})\zeta^\alpha(\mathcal{U})\mathcal{S}^\alpha(\mathbf{x}, p^g - p^l),$$

and the mobility of the component i in phase α defined by

$$m_i^\alpha(\mathbf{x},\mathcal{U}) = c_i^\alpha(\mathcal{U})\zeta^\alpha(\mathcal{U})\frac{k_r^\alpha(\mathbf{x}, \mathcal{S}^\alpha(\mathbf{x}, p^g - p^l))}{\mu^\alpha(\mathcal{U})}.$$

In the free flow domain, it is assumed that the gas molar and mass densities are fixed which amounts to neglect the effect of the pressure and molar fraction variations on the gas densities. It is assumed that the coupling with the porous medium induces a small perturbation of a given stationary turbulent flow with velocity $\mathbf{u}_t$ and pressure p_t solution of the following RANS model

$$\begin{cases} \rho^g\mathrm{div}\Big(\mathbf{u}_t\otimes\mathbf{u}_t\Big) + \mathrm{div}\Big(-(\mu^g+\mu_t)(\nabla\mathbf{u}_t + \nabla^t\mathbf{u}_t)\Big) + \nabla p_t = \rho^g\mathbf{g} \text{ on } \Omega^g, \\ \mathrm{div}(\mathbf{u}_t) = 0 \text{ on } \Omega^g, \end{cases} \tag{2}$$

with boundary condition $\mathbf{u}_t = 0$ at the interface Γ. In (2), μ_t is the turbulent viscosity which is modelled e.g. using an algebraic turbulent model or a more advanced $k-\epsilon$ model. Note that this turbulent viscosity μ_t vanishes at the interface Γ but is much larger than μ^g away from the viscous boundary layer. This turbulent flow is responsible for a turbulent diffusion denoted by D_t and typically given by $D_t = \dfrac{1}{S_c}\dfrac{\mu_t}{\rho^g}$ where S_c is the Schmidt number (see e.g. [5]). This turbulent diffusion, which is much larger than D^g away from the viscous boundary layer, plays an essential role in the order of magnitude of the evaporation rate. The gas molar fraction of the uncoupled flow corresponds to the initial condition $c = c_{init}$ of the coupled flow.

The coupling of the free flow with the porous medium flow leads to the new gas velocity $\mathbf{u} = \mathbf{u}_t + \tilde{\mathbf{u}}$, the new pressure $p = p_t + \tilde{p}$, and the gas molar fraction c solutions of the following RANS compositional model

$$\begin{cases} \rho^g\mathrm{div}\Big(\mathbf{u}_t\otimes\tilde{\mathbf{u}} + \tilde{\mathbf{u}}\otimes\mathbf{u}_t + \tilde{\mathbf{u}}\otimes\tilde{\mathbf{u}}\Big) \\ \qquad -\mathrm{div}\Big((\mu^g+\mu_t))(\nabla\tilde{\mathbf{u}} + \nabla^t\tilde{\mathbf{u}})\Big) + \nabla\tilde{p} = 0 & \text{on } \Omega^g\times(0,T), \\ \partial_t c_i + \mathrm{div}\Big(c_i\mathbf{u}\Big) + \mathrm{div}(-(D^g + D_t)\nabla c_i) = 0, i\in\mathcal{C} & \text{on } \Omega^g\times(0,T), \\ \sum_{i\in\mathcal{C}} c_i = 1 & \text{on } \Omega^g\times(0,T). \end{cases} \tag{3}$$

Due to the small perturbation assumption, the turbulent viscosity μ_t and diffusion D_t are assumed in (3) to be given functions of $\mathbf{x}$ independent on $\tilde{\mathbf{u}}$, $\tilde{p}$, and c. A stationary model for the momentum equation is used in (3) due to the much larger porous medium flow time scale than the free flow time scale. The component molar conservations in the free flow domain are kept unstationary in order to ease the non linear solution of the coupled system at the start of the simulation.

At the interface Γ between the free flow domain and the porous medium the coupling conditions are an adaptation to those stated in [23]. The Beavers Joseph condition at the interface Γ is replaced by a no slip condition due to the low permeability of the porous medium. The remaining conditions are the continuity of the molar normal flux for each component $i \in \mathcal{C}$ assuming that the liquid phase is instantaneously vaporized, the continuity of the gas molar fractions, the continuity of the normal component of the normal stress, and the gas liquid thermodynamical equilibrium. We obtain the following interface conditions

$$\begin{cases} \dfrac{1}{\zeta^g} \displaystyle\sum_{\alpha=l,g} -m_i^\alpha(\mathbf{x},\mathcal{U})\mathbf{K}\Big(\nabla p^\alpha - \rho^\alpha(\mathcal{U})\mathbf{g}\Big)\cdot\mathbf{n} = c_i\mathbf{u}\cdot\mathbf{n} - D^g\nabla c_i\cdot\mathbf{n},\ i\in\mathcal{C} & \text{on } \Gamma\times(0,T), \\ c_i^g(\mathcal{U}) = c_i, i\in\mathcal{C} & \text{on } \Gamma\times(0,T), \\ p^g = p + \mathbf{n}\cdot\Big(\rho^g\mathbf{u}\otimes\mathbf{u} - \mu^g(\nabla\mathbf{u}+\nabla^t\mathbf{u})\Big)\mathbf{n} & \text{on } \Gamma\times(0,T), \\ \displaystyle\sum_{i\in\mathcal{C}} c_i^\alpha(\mathcal{U}) = 1\ \alpha = g,l, & \text{on } \Gamma\times(0,T), \\ \mathbf{u}\wedge\mathbf{n} = 0 & \text{on } \Gamma\times(0,T), \end{cases} \tag{4}$$

where $\mathbf{n}$ denotes the unit normal vector at the interface Γ oriented outward of the porous medium domain. Note that in practice, the gas pressure jump $p - p^g$ at the interface can be neglected since a small flow rate between the porous medium and the free flow domain is expected.

2.2 Splitting algorithm

In [3, 17, 22] all the Darcy and free flow unknowns corresponding in our case to $\mathcal{U}$, $\mathbf{u}$, p and c are solved using a monolithic Newton algorithm at each time step of a fully implicit Euler time integration scheme. Given the complexity of the full system, this approach naturally leads to difficulties in solving the non linear and linearized systems.

Alternatively, many coupling strategies simply rely on a sequential coupling algorithm of Dirichlet Neumann type using typically two different codes for the Darcy and free flows. This type of sequential coupling algorithm leads to very small time steps due to the strong coupling between the liquid pressure p^l and the water molar fraction c_e at the interface Γ which is induced by the thermodynamical equilibrium. For example, in [12, 10], a time step of 0.1 s is reported resulting in roughly 100h of CPU time for a few days of simulation. We refer to [11] for a recent review including a list of codes implementing sequential or fully implicit coupling algorithms for the modelling of drying processes at the interface between a porous medium and a free flow domain.

Our approach is rather to split the system in two simpler subsystems at each time step of the fully implicit Euler time integration scheme. In a first step, for given $\mathbf{u}$ and p in Ω^g, the strongly coupled unknowns $\mathcal{U}$ in Ω^p, c in Ω^g, and $\mathbf{u}\cdot\mathbf{n}$ at Γ are computed using a Newton algorithm solving the Darcy flow in the porous medium together with the tracer equations in the free flow domain and part of the interface conditions. The gas velocity $\mathbf{u}$ and gas pressure p in Ω^g are then computed in a second step solving the momentum and divergence free equations using step 1 normal velocity $\mathbf{u}\cdot\mathbf{n}$ at the interface Γ. The two steps 1 and 2 are iterated, as a fixed point algorithm for the normal velocity $\mathbf{u}\cdot\mathbf{n}$ at the interface Γ, until the stopping criteria $\|1 - \sum_{i\in\mathcal{C}} c_i\|_{L^\infty(\Omega^g)} \leq \epsilon$ is satisfied for a

given accuracy ϵ. The convergence of this fixed point method is expected to be very fast due to the weak coupling of the unknowns $\mathcal{U}$, c, and $\mathbf{u}\cdot\mathbf{n}$ to the unknowns $\mathbf{u}$ and p. We will see in the numerical Section 4 that, in practice, the sequential version of this algorithm, i.e. a single fixed point iteration, suffices to obtain a very accurate result.

We detail below the two steps of the splitting algorithm at a given time step Δt^n between times t^{n-1} and t^n, which are iterated until convergence of the gas molar fractions such that $\|1 - \sum_{i\in\mathcal{C}} c_i\|_{L^\infty(\Omega^g)} \leq \epsilon$. To fix idea, an Euler implicit time integration is used in both domains. The unknowns at time n are denoted with the n superscript. The fixed point iteration count is denoted by k and the splitting algorithm is initialized with the previous time step solution.

Step 1: it computes $\mathcal{U}^{n,k}$ in the porous medium, $c^{n,k}$ in the free flow domain and $\mathbf{u}^{n,k}\cdot\mathbf{n}$ at the interface, at fixed velocity $\mathbf{u}^{n,k-1}$ and pressure $p^{n,k-1}$ in the free flow domain, as the solution of the system coupling the Darcy flow model

$$\left\{\begin{array}{ll} \phi\dfrac{n_i(\mathbf{x},\mathcal{U}^{n,k}) - n_i(\mathbf{x},\mathcal{U}^{n-1})}{\Delta t^n} & \\ +\mathrm{div}\Big(\displaystyle\sum_{\alpha=g,l} -m_i^\alpha(\mathbf{x},\mathcal{U}^{n,k})\mathbf{K}\Big(\nabla p^{\alpha,n,k} - \rho^\alpha(\mathcal{U}^{n,k})\mathbf{g}\Big)\Big) = 0,\ i\in\mathcal{C} & \text{on } \Omega^p, \\ \displaystyle\sum_{i\in\mathcal{C}} c_i^\alpha(\mathcal{U}^{n,k}) = 1,\ \alpha = g,l & \text{on } \Omega^p, \end{array}\right. \tag{5}$$

with the tracer equations in the free flow model

$$\frac{c_i^{n,k} - c_i^{n-1}}{\Delta t^n} + \mathrm{div}\Big(c_i^{n,k}\mathbf{u}^{n,k-1}\Big) + \mathrm{div}(-(D^g + D_t)\nabla c_i^{n,k}) = 0, i\in\mathcal{C}, \quad \text{on } \Omega^g, \tag{6}$$

and the following subset of the interface conditions

$$\left\{\begin{array}{ll} \dfrac{1}{\zeta^g}\displaystyle\sum_{\alpha=l,g} -m_i^\alpha(\mathbf{x},\mathcal{U}^{n,k})\mathbf{K}\Big(\nabla p^{\alpha,n,k} - \rho^\alpha(\mathcal{U}^{n,k})\mathbf{g}\Big)\cdot\mathbf{n} = c_i^{n,k}\mathbf{u}^{n,k}\cdot\mathbf{n} - D^g\nabla c_i^{n,k}\cdot\mathbf{n},\ i\in\mathcal{C} & \text{on } \Gamma, \\ c_i^g(\mathcal{U}^{n,k}) = c_i^{n,k}, i\in\mathcal{C} & \text{on } \Gamma, \\ p^{g,n,k} = p^{n,k-1} + \mathbf{n}\cdot\Big(\rho^g\mathbf{u}^{n,k-1}\otimes\mathbf{u}^{n,k-1} - \mu^g(\nabla\mathbf{u}^{n,k-1} + \nabla^t\mathbf{u}^{n,k-1})\Big)\mathbf{n} & \text{on } \Gamma, \\ \displaystyle\sum_{i\in\mathcal{C}} c_i^\alpha(\mathcal{U}^{n,k}) = 1\,\alpha = g,l, & \text{on } \Gamma. \end{array}\right. \tag{7}$$

Note that in (6) and (7), the normal gas velocity $\mathbf{u}^{n,k}\cdot\mathbf{n}$ is used for the convective flux at the interface Γ and not $\mathbf{u}^{n,k-1}\cdot\mathbf{n}$.

Step 2: Given the normal gas velocity $\mathbf{u}^{n,k}\cdot\mathbf{n}$ at the interface Γ computed at step 1, step 2 computes the gas velocity $\mathbf{u}^{n,k} = \mathbf{u}_t + \tilde{\mathbf{u}}^{n,k}$ and the gas pressure $p^{n,k} = p_t + \tilde{p}^{n,k}$ as the solution at time t^n of the following RANS model

$$\left\{\begin{array}{ll} \rho^g\mathrm{div}\Big(\mathbf{u}_t\otimes\tilde{\mathbf{u}}^{n,k} + \tilde{\mathbf{u}}^{n,k}\otimes\mathbf{u}_t + \tilde{\mathbf{u}}^{n,k}\otimes\tilde{\mathbf{u}}^{n,k}\Big) & \\ \qquad -\mathrm{div}\Big((\mu^g + \mu_t)(\nabla\tilde{\mathbf{u}}^{n,k} + \nabla^t\tilde{\mathbf{u}}^{n,k})\Big) + \nabla\tilde{p}^{n,k} = 0 & \text{on } \Omega^g, \\ \mathrm{div}(\tilde{\mathbf{u}}^{n,k}) = 0 & \text{on } \Omega^g. \end{array}\right. \tag{8}$$

3 Reduced model

It is assumed to fix ideas that the free flow domain is a cylindrical domain of length L and of section S with S an open simply connected subdomain of $\mathbb{R}^2$. The free flow domain is defined by

$\Omega^g = (0, L) \times S$ and the interface by $\Gamma = (0, L) \times \partial S$. In the following, γ denotes the trace operator on Γ and s is the curvilinear coordinate along ∂S.

The reduced model is motivated by the large longitudinal dimension compared with the transversal dimensions of the free flow domain in radioactive waste geological storage applications. It is assumed that the pressure p and the longitudinal velocity u in the section S depend only on the longitudinal coordinate x and on time t. The gas molar fraction c is also assumed to depend only on x and t. At the interface Γ, the gas molar fraction in the viscous boundary layer is given by $c^g(\gamma\mathcal{U})$ from the gas molar fraction continuity. From the gas pressure continuity condition, the free flow pressure p of the reduced model is given by γp^g. Another unknown is the normal gas velocity at the interface Γ averaged along ∂S. It is denoted by v_I with the normal oriented outward of the porous medium.

3.1 Reduced 1D model in the free flow domain

The new system amounts to find the porous medium unknowns $\mathcal{U}(\mathbf{x}, t)$ on $\Omega^p \times (0, T)$, and the free flow domain unknowns $u(x, t)$, $c(x, t)$ on $(0, L) \times (0, T)$ and $v_I(\mathbf{x}, t)$ on $\Gamma \times (0, T)$ satisfying the Darcy flow system (1), coupled with the following modified system at the interface Γ

$$\left\{\begin{array}{l} c_i^g(\gamma\mathcal{U})v_I^+ + c_i v_I^- + \dfrac{D^g}{\delta}(c_i^g(\gamma\mathcal{U}) - c_i) \\ = \dfrac{1}{\zeta^g}\displaystyle\sum_{\alpha=g,l} -m_i^\alpha(\mathbf{x},\mathcal{U})\mathbf{K}\Big(\nabla p^\alpha - \rho^\alpha(\mathcal{U})\mathbf{g}\Big)\cdot\mathbf{n},\ i \in \mathcal{C} \text{ on } \Gamma \times (0, T), \\ \displaystyle\sum_{i\in\mathcal{C}} c_i^\alpha(\gamma\mathcal{U}) = 1,\ \alpha = g, l \text{ on } \Gamma \times (0, T), \\ \gamma p^g = p, \text{ on } \Gamma \times (0, T), \end{array}\right. \tag{9}$$

and with the conservation equations along the free flow domain

$$\left\{\begin{array}{l} \partial_t c_i + \partial_x(c_i u) \\ = \dfrac{1}{|S|\zeta^g}\displaystyle\int_{\partial S}\sum_{\alpha=g,l} -m_i^\alpha(\mathbf{x},\mathcal{U})\mathbf{K}\Big(\nabla p^\alpha - \rho^\alpha(\mathcal{U})\mathbf{g}\Big)\cdot\mathbf{n}\ ds,\ i \in \mathcal{C} \text{ on } (0, L) \times (0, T), \\ \displaystyle\sum_{i\in\mathcal{C}} c_i = 1 \text{ on } (0, L) \times (0, T). \end{array}\right. \tag{10}$$

To fix ideas the pressure drop is given by the Forchheimer model $(\alpha_g u + \beta_g |u| u) = -\partial_x \gamma p^g$ with $\alpha_g \geq 0$ and $\beta_g \geq 0$, $\alpha_g + \beta_g > 0$. In (9), we have used the notation $a^+ = \max(a, 0)$ and $a^- = \min(a, 0)$. The function $\delta > 0$ corresponds to the molar fraction boundary layer thickness that need to be modelled as discussed in the next subsection.

3.2 Molar fraction boundary layer thickness model

A simple choice of the boundary layer thickness δ is given by the following model. let $\mathcal{L}$ denote the stationary convection diffusion operator defined for all $d \in H^1(\Omega^g)$ by

$$\mathcal{L}d = \mathrm{div}\Big(\mathbf{u}_t d - (D^g + D_t)\nabla d\Big),$$

recalling that $\mathrm{div}(\mathbf{u}_t) = 0$ and that $\mathbf{u}_t = 0$ on Γ. We define the solution d of the following stationary convection diffusion equation given a constant boundary condition $d_{in} \in \mathbb{R}$ on $\Gamma_{in}^g = \{0\} \times S$ and a

boundary condition $d_\Gamma \in H^{\frac{1}{2}}(\Gamma)$ on Γ:

$$\left\{\begin{array}{rl} \mathcal{L}d = 0 & \text{on } \Omega^g, \\ d = d_\Gamma & \text{on } \Gamma, \\ d = d_{in} & \text{on } \Gamma^g_{in}, \\ \nabla d \cdot \mathbf{n} = 0 & \text{on } \Gamma^g_{out} = \{L\} \times S. \end{array}\right. \tag{11}$$

Let us denote by $\mathcal{S}_P$ the linear Steklov-Poincaré operator such that for all $d_\Gamma \in H^{\frac{1}{2}}(\Gamma)$

$$\mathcal{S}_P(d_\Gamma - d_{in}) = -\nabla d \cdot \mathbf{n} \in H^{-\frac{1}{2}}(\Gamma),$$

and let us denote by M the linear compact operator from $H^{\frac{1}{2}}(\Gamma)$ to $H^{\frac{1}{2}}(\Gamma)$ such that for all $d_\Gamma \in H^{\frac{1}{2}}(\Gamma)$

$$M(d_\Gamma - d_{in}) = -d_{in} + \frac{1}{|S|}\int_S d(.,y,z)dydz \in H^1(\Gamma).$$

Then, we define for $d_{in} \in \mathbb{R}$, $d_\Gamma = d_\gamma 1_\Gamma$ with $d_\gamma \in \mathbb{R}$, $d_{in} \neq d_\gamma$,

$$\delta = \frac{d_\Gamma - \frac{1}{|S|}\int_S d(.,y,z)dydz}{-\nabla d \cdot \mathbf{n}} = \frac{(I-M)1_\Gamma}{\mathcal{S}_P 1_\Gamma}$$

where 1_Γ denotes the function equal to 1 on Γ. This definition of δ is clearly independent on the choice of both d_γ and d_{in}. Also from the maximum principle, $\delta(\mathbf{x}) > 0$ for all $\mathbf{x} \in \Gamma$.

From the maximum principle and the Fredholm alternative, the linear operator $I - M$ defines a bijection from $H^{\frac{1}{2}}(\Gamma)$ to $H^{\frac{1}{2}}(\Gamma)$. Hence we can define the operator

$$\overline{\mathcal{S}}_P = \mathcal{S}_P(I-M)^{-1},$$

which relates the normal flux at Γ to the difference between the trace on Γ and the section mean values as follows

$$-\nabla d \cdot \mathbf{n} = \overline{\mathcal{S}}_P\Big(d_\Gamma - \frac{1}{|S|}\int_S d(.,y,z)dydz\Big).$$

In this framework, $\dfrac{1}{\delta}$ clearly appears as a diagonal approximation of the operator $\overline{\mathcal{S}}_P$ which is built to be exact for constant boundary conditions on Γ. A better approximation could be obtained using a second order approximation of the operator $\overline{\mathcal{S}}_P$ following the techniques used in Optimized Schwarz Methods [18].

It is more usual to relate the flux to the difference between the trace on Γ and d_{in} using the Steklov Poincaré operator. The diagonal approximation $\frac{D^g}{\delta} = D^g\mathcal{S}_P 1_\Gamma$ of the operator $D^g\mathcal{S}_P$ is refered to as the Convective Mass Transfer Coefficient $CMTC$ (see the review [11] and the references there in for a discussion about CMTCs). In our context, our choice has the advantage to take into account the coupling of the interface conditions with the 1D gas free flow.

4 Numerical tests

In order to assess the efficiency of the splitting algorithm and to compare the full and reduced models, we consider in the following tests a simple 2D setting with $\Omega^g = (0,L)\times(0,H_1)$, $\Omega^p = (0,L)\times(H_1,H_2)$ and $\Gamma = (0,L)\times\{H_1\}$. Figure 1 exhibits the two domains, the interface Γ and the external boundaries Γ^p_D, Γ^p_N, Γ^g_{in}, Γ^g_{out}, and Γ^g_N. We consider the set of components $\mathcal{C} = \{e, a\}$ where e denotes the water

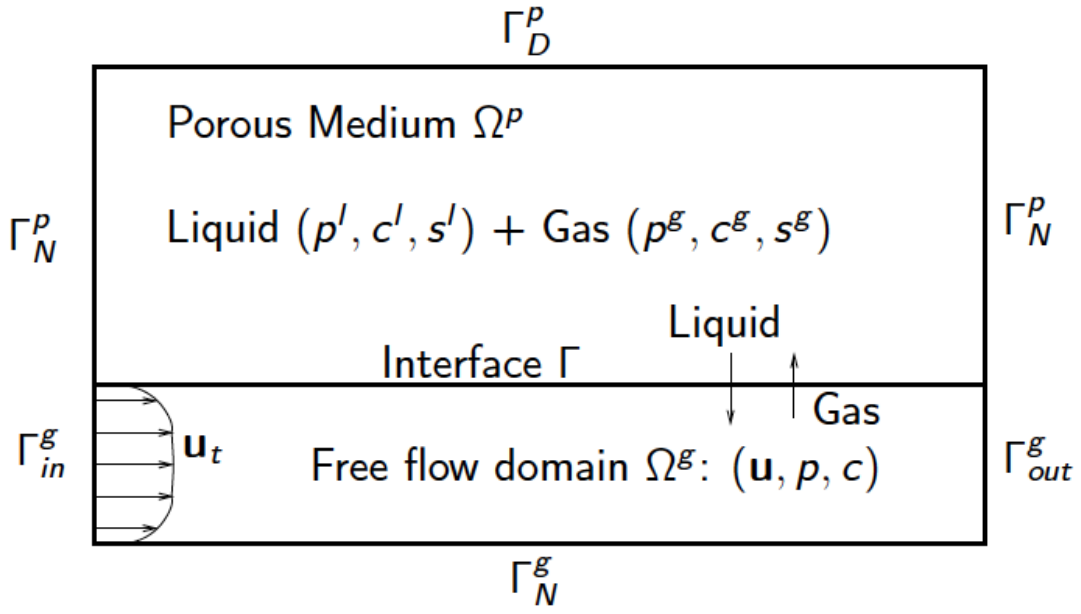

Figure 1: Free flow domain Ω^g, porous medium domain Ω^p, interface Γ, and remaining boundaries for our 2D test case.

component, and a the gaseous air component with the fixed Henry constant $H_a = 6\ 10^9$ Pa. The gas molar density is given by $\zeta^g(p^g) = \frac{p^g}{RT_e}$ mol.m^{-3}, and the liquid molar density is fixed to $\zeta^l = 55555$ mol.m^{-3}. The phase viscosities are fixed to $\mu^g = 18.51\ 10^{-6}$ Pa.s^{-1} and $\mu^l = 10^{-3}$ Pa.s^{-1}. The mass densities are defined by $\rho^\alpha = \zeta^\alpha \sum_{i\in\mathcal{C}} c_i^\alpha M_i$ with the molar masses of the components $M_a = 29\ 10^{-3}$ Kg, $M_e = 18\ 10^{-3}$ Kg.

The fugacities of the components in the gas phase are given by Dalton's law for an ideal mixture of perfect gas $f_i^g = c_i^g p^g$, $i = e, a$. The fugacities of the components in the liquid phase are given by Henry's law for the dissolution of the air component in the liquid phase $f_a^l = c_a^l H_a$, and by Raoult-Kelvin's law for the water component in the liquid phase $f_e^l = c_e^l P_{sat}(T_e)\exp\Big(\frac{-(p^g-p^l)}{\zeta^l RT_e}\Big)$, where $P_{sat}(T_e)$ is the vapour pressure of the pure water.

The solution of the equation $f^\alpha(c^\alpha, p^g, p^l) = f$ leads to the following component molar fractions c_i^α as functions of $\mathcal{U}$:

$$\begin{cases} c_e^l(\mathcal{U}) = \dfrac{f_e}{P_{sat}(T_e)}\exp\Big(\dfrac{(p^g-p^l)}{\zeta^l RT_e}\Big), & c_a^l(\mathcal{U}) = \dfrac{f_a}{H_a}, \\ c_e^g(\mathcal{U}) = \dfrac{f_e}{p^g}, & c_a^g(\mathcal{U}) = \dfrac{f_a}{p^g}. \end{cases} \tag{12}$$

The relative permeabilities and capillary pressure in the porous medium are given by the following Van-Genuchten laws

$$k_r^l(s^l) = \begin{cases} 0 & \text{if} \quad s^l < s_r^l, \\ 1 & \text{if} \quad s^l > 1 - s_r^g, \\ \sqrt{\bar{s}^l}\Big(1 - (1 - (\bar{s}^l)^{1/m})^m\Big)^2 & \text{if} \quad s_r^l \le s^l \le 1 - s_r^g, \end{cases}$$

$$k_r^g(s^g) = \begin{cases} 0 & \text{if} \quad s^g < s_r^g, \\ 1 & \text{if} \quad s^g > 1 - s_r^l, \\ \sqrt{1-\bar{s}^l}\Big(1 - (\bar{s}^l)^{1/m}\Big)^{2m} & \text{if} \quad s_r^g \le s^g \le 1 - s_r^l, \end{cases}$$

and

$$s^l(-p_c) = s_r^l + (1 - s_r^l - s_r^g)\frac{1}{\left(1 + (\frac{p_c}{P_r})^n\right)^m},$$

with

$$\bar{s}^l = \frac{s^l - s_r^l}{1 - s_r^l - s_r^g}.$$

In our numerical tests, the stationary turbulent profile, corresponding to the velocity without the coupling with the porous medium, is obtained using the following Prandtl algebraic turbulent model for the turbulent viscosity (see [28, 7, 5])

$$\mu_t = \rho^g (l_m(y))^2 |u_t'(y)|, \;\; l_m(y) = 0.41 \min(y, H_1 - y).$$

It leads to compute the solution $(\mathbf{u}_t, p_t)$ with $\mathbf{u}_t(y) = \begin{pmatrix} u_t(y) \\ 0 \end{pmatrix}$ of the system

$$\left\{ \begin{array}{rl} \mathrm{div}(-(\mu^g + \mu_t)\nabla u_t) + \partial_x p_t = 0 & \text{on } \Omega^g, \\ \partial_y p_t = -\rho^g g & \text{on } \Omega^g, \\ \mathrm{div}(\mathbf{u}_t) = 0 & \text{on } \Omega^g, \end{array} \right. \tag{13}$$

which reduces to the following Ordinary Differential Equation (ODE) for $u_t(y)$

$$(\mu^g + \rho^g (l_m(y))^2 |u_t'|) u_t' = \alpha_t (H_1/2 - y),$$

to be integrated between $y = 0$ and $y = \frac{H_1}{2}$ by symmetry. The integration constant of this ODE and the constant α_t are obtained using the conditions $u_t(0) = 0$ and

$$\frac{1}{H_1} \int_0^{H_1} u_t(y) dy = w_{in},$$

where w_{in} is the prescribed mean value of the input velocity. Using the outflow boundary condition (14) specified below, the turbulent pressure is defined by

$$p_t(x, y) = p_{out} - \rho^g g y - \alpha_t (x - L),$$

where p_{out} is the outflow pressure for $y = 0$, and $g = 9.81 m.s^{-2}$ is the gravity acceleration. In our numerical tests, the turbulent diffusion is related to the turbulent viscosity by

$$D_t(y) = \frac{\mu_t(y)}{\rho^g},$$

corresponding to a Schmidt number of 1 to fix ideas. The porous medium is initially saturated by the liquid phase with imposed pressure p_{init}^l and composition $c_{a,init}^l = 0$, $c_{e,init}^l = 1$ which combined with the equation $c_e^g(\mathcal{U}_{init}) + c_a^g(\mathcal{U}_{init}) = 1$ defines the initial unknowns $\mathcal{U}_{init}$. At the top porous medium boundary Γ_D^p, a Dirichlet boundary condition is imposed equal to the initial condition $\mathcal{U}_D = \mathcal{U}_{init}$. At both sides Γ_N^p of the porous medium, a zero normal flux boundary condition is imposed for all components. The initial condition in the free flow domain is given by $p_{init} = 10^5$ Pa and $c_{e,init} = 1 - c_{a,init}$ defined by the prescribed relative humidity

$$H_{r,init} = \frac{c_{e,init} p_{init}}{P_{sat}(T_e)}.$$

At the boundary Γ^g_{in}, the input molar fractions are set to $c_{in} = c_{init}$, and the stationary turbulent profile $\mathbf{u}_t(y)$ is imposed. At the boundary Γ^g_{out}, the following outflow boundary conditions are imposed

$$p - (\mu^g + \mu_t(y))\partial_x u = p^{out} - \rho^g g y, \quad \partial_x v = 0, \tag{14}$$

with $p_{out} = p_{init}$. The usual gradient is used in this outflow condition rather than the symmetric gradient in such a way that this condition can be satisfied by $(\mathbf{u}_t, p_t)$. The diffusive normal fluxes are set to zero for all components $i \in \mathcal{C}$ on Γ^g_{out}. At the bottom boundary Γ^g_N, the velocity $\mathbf{u}$ is set to zero as well as the diffusive normal fluxes for all components $i \in \mathcal{C}$.

4.1 Finite Volume Discretization on a Cartesian mesh

The domain $(0, L) \times (0, H_2)$ is discretized by a non uniform Cartesian mesh refined at both sides of the interface Γ. A finite volume cell centered discretization with a Two Point Flux Approximation (TPFA) of the Darcy fluxes and an upwindind of the mobility terms is used for the porous medium flow [25, 2]. For the free flow, a staggered MAC (Marker-And-Cell) scheme is used for the Navier Stokes equations [16, 24, 30] combined with a TPFA discretization of the diffusion fluxes.

4.1.1 TPFA discretization of Step 1

To write the discretization of the step 1 model, it is convenient to use the following unstructured mesh notations. Let $\mathcal{M}^p$ (resp. $\mathcal{M}^g$) denotes the set of cells of Ω^p (resp. Ω^g). The set of edges of the mesh is denoted by $\mathcal{E}$, $\mathcal{M}_\sigma \subset \mathcal{M}^p \cup \mathcal{M}^g$ stands for the set of cells sharing the edge σ, and $\mathcal{E}_K$ denote the set of edges of the cell $K \in \mathcal{M}^p \cup \mathcal{M}^g$. The set of edges $\mathcal{E}$ is partitioned as follows:

$\mathcal{E}^p_{int}$ the set of interior edges of Ω^p with $\mathcal{M}_\sigma = \{K, L\} \subset \mathcal{M}^p$ for all $\sigma \in \mathcal{E}^p_{int}$,

$\mathcal{E}^p_\flat$ the set of edges of $\Gamma^p_\flat$ with $\mathcal{M}_\sigma = \{K\} \subset \mathcal{M}^p$ for all $\sigma \in \mathcal{E}^p_\flat$ with $\flat = D$ or N,

$\mathcal{E}_\Gamma$ the set of edges of Γ with $\mathcal{M}_\sigma = \{K, L\}$, $K \in \mathcal{M}^p$, $L \in \mathcal{M}^g$ for all $\sigma \in \mathcal{E}_\Gamma$,

$\mathcal{E}^g_{int}$ the set of interior edges of Ω^g with $\mathcal{M}_\sigma = \{K, L\} \subset \mathcal{M}^g$ for all $\sigma \in \mathcal{E}^g_{int}$

$\mathcal{E}^f_\flat$ the set of edges of $\Gamma^f_\flat$ with $\mathcal{M}_\sigma = \{K\} \subset \mathcal{M}^g$ for all $\sigma \in \mathcal{E}^f_\flat$, $\flat = in, out, N$.

The set of discrete unknowns is denoted by $\mathcal{U}_K = (p^g_K, p^l_K, f_K) \in \mathbb{R}^{\mathcal{C}+2}$, $K \in \mathcal{M}^p$ in the porous medium, by $c_K \in \mathbb{R}^{\mathcal{C}}$, $K \in \mathcal{M}^g$ in the free flow domain, and by $\mathcal{U}_\sigma = (p^g_\sigma, p^l_\sigma, f_\sigma) \in \mathbb{R}^{\mathcal{C}+2}$ and $v_{I,\sigma} \in \mathbb{R}$ for all edges $\sigma \in \mathcal{E}_\Gamma$ at the interface where $v_{I,\sigma}$ is the normal gas velocity oriented outward of the free flow domain.

Let ϕ_K denote the mean porosity in the cell K. Let $\mathbf{x}_K = (x_K, y_K)$ denote the center of the cell K and $\mathbf{x}_\sigma = (x_\sigma, y_\sigma)$ the center of the edge σ, and let T_σ be the TPFA Darcy transmissibility of the edge σ. The TPFA Darcy fluxes at the interior edges $\sigma \in \mathcal{E}^p_{int}$ of the porous medium, oriented outward to the cell K with $\mathcal{M}_\sigma = \{K, L\}$ are defined for $\alpha = g, l$ by

$$V^\alpha_{K,\sigma}(\mathcal{U}_K, \mathcal{U}_L) = T_\sigma\Big(p^\alpha_K - p^\alpha_L + \rho^\alpha(\frac{\mathcal{U}_K + \mathcal{U}_L}{2})g(y_K - y_L)\Big).$$

Similarly, at the edges $\sigma \in (\mathcal{E}^p_D \cup \mathcal{E}_\Gamma) \cap \mathcal{E}_K$, $K \in \mathcal{M}^p$, they are defined for $\alpha = g, l$ by

$$V^\alpha_{K,\sigma}(\mathcal{U}_K, \mathcal{U}_\sigma) = T_\sigma\Big(p^\alpha_K - p^\alpha_\sigma + \rho^\alpha(\frac{\mathcal{U}_K + \mathcal{U}_\sigma}{2})g(y_K - y_\sigma)\Big),$$

Then, using an upwind approximation of the mobilities with respect to the sign of each phase Darcy flux, we set for all $\sigma \in \mathcal{E}_{int}^p$, $\mathcal{M}_\sigma = \{K, L\}$

$$V_{K,\sigma}^{\alpha,i}(\mathcal{U}_K, \mathcal{U}_L) = m_i^\alpha(\mathbf{x}_K, \mathcal{U}_K) V_{K,\sigma}^\alpha(\mathcal{U}_K, \mathcal{U}_L)^+ + m_i^\alpha(\mathbf{x}_L, \mathcal{U}_L) V_{K,\sigma}^\alpha(\mathcal{U}_K, \mathcal{U}_L)^-, \tag{15}$$

and for all $\sigma \in (\mathcal{E}_D^p \cup \mathcal{E}_\Gamma) \cap \mathcal{E}_K$, $K \in \mathcal{M}^p$

$$V_{K,\sigma}^{\alpha,i}(\mathcal{U}_K, \mathcal{U}_\sigma) = m_i^\alpha(\mathbf{x}_K, \mathcal{U}_K) V_{K,\sigma}^\alpha(\mathcal{U}_K, \mathcal{U}_\sigma)^+ + m_i^\alpha(\mathbf{x}_K, \mathcal{U}_\sigma) V_{K,\sigma}^\alpha(\mathcal{U}_K, \mathcal{U}_\sigma)^-. \tag{16}$$

The discrete conservation equations in the porous medium writes for all cells $K \in \mathcal{M}^p$

$$\begin{cases} \phi_K |K| \dfrac{n_i(\mathbf{x}_K, \mathcal{U}_K^{n,k}) - n_i(\mathbf{x}_K, \mathcal{U}_K^{n-1})}{\Delta t^n} + \displaystyle\sum_{\alpha=l,g} \Big(\sum_{\sigma \in \mathcal{E}_{int}^p \cap \mathcal{E}_K} V_{K,\sigma}^{\alpha,i}(\mathcal{U}_K^{n,k}, \mathcal{U}_L^{n,k}) \\ \qquad + \displaystyle\sum_{\sigma \in \mathcal{E}_D^p \cap \mathcal{E}_K} V_{K,\sigma}^{\alpha,i}(\mathcal{U}_K^{n,k}, \mathcal{U}_D) + \sum_{\sigma \in \mathcal{E}_\Gamma \cap \mathcal{E}_K} V_{K,\sigma}^{\alpha,i}(\mathcal{U}_K^{n,k}, \mathcal{U}_\sigma^{n,k}) \Big) = 0, \ i \in \mathcal{C} \\ \displaystyle\sum_{i \in \mathcal{C}} c_i^\alpha(\mathcal{U}_K^{n,k}) = 1, \ \alpha = g, l, \end{cases} \tag{17}$$

with $|K|$ denoting the volume of the cell K.

The normal gas velocities at the edges of the free flow domain are given by the step 2 at the fixed point iteration $k-1$ and denoted for all $\sigma \in \mathcal{E}_K \setminus \mathcal{E}_\Gamma$, $K \in \mathcal{M}^g$ by $\mathbf{u}^{n,k-1} \cdot \mathbf{n}_{K,\sigma}$, where $\mathbf{n}_{K,\sigma}$ is the unit normal vector at the edge σ outward to the cell K. The cell pressures $p_K^{n,k-1}$ for all $K \in \mathcal{M}^g$ are also given by the step 2 at the fixed point iteration $k-1$. The discretization of the tracer equation writes for all cells $K \in \mathcal{M}^g$ and all component $i \in \mathcal{C}$:

$$\begin{aligned} & \frac{c_{i,K}^{n,k} - c_{i,K}^{n-1}}{\Delta t^n} |K| \\ & + \sum_{\sigma \in \mathcal{E}_{int}^g \cap \mathcal{E}_K} \Big(c_{i,K}^{n,k} |\sigma| (\mathbf{u}^{n,k-1} \cdot \mathbf{n}_{K,\sigma})^+ + c_{i,L}^n |\sigma| (\mathbf{u}^{n,k-1} \cdot \mathbf{n}_{K,\sigma})^- + T_\sigma^D (c_{i,K}^{n,k} - c_{i,L}^{n,k}) \Big) \\ & + \sum_{\sigma \in \mathcal{E}_\Gamma \cap \mathcal{E}_K} \Big(\bar{c}_{i,K}^{n,k} |\sigma| (v_{I,\sigma}^{n,k})^+ + c_i^g(\mathcal{U}_\sigma^{n,k}) |\sigma| (v_{I,\sigma}^{n,k})^- + T_\sigma^D (\bar{c}_{i,K}^{n,k} - c_i^g(\mathcal{U}_\sigma^{n,k})) \Big) \\ & + \sum_{\sigma \in \mathcal{E}_{in}^g \cap \mathcal{E}_K} \Big(c_{i,K}^{n,k} |\sigma| (\mathbf{u}^{n,k-1} \cdot \mathbf{n}_{K,\sigma})^+ + c_{i,in} |\sigma| (\mathbf{u}^{n,k-1} \cdot \mathbf{n}_{K,\sigma})^- + T_\sigma^D (c_{i,K}^{n,k} - c_{i,in}) \Big) \\ & + \sum_{\sigma \in \mathcal{E}_{out}^g \cap \mathcal{E}_K} c_{i,K}^{n,k} |\sigma| (\mathbf{u}^{n,k-1} \cdot \mathbf{n}_{K,\sigma})^+ = 0, \end{aligned} \tag{18}$$

where $|\sigma|$ is the length of the edge σ, T_σ^D is the diffusion TPFA transmissibility of the edge σ, and where $\bar{c}_i = \frac{c_i}{\sum_{j \in \mathcal{C}} c_j}, i \in \mathcal{C}$ stands for the normalized molar fractions.

The discrete conservation equations in the porous medium domain (17) and in the free flow domain (18) are coupled to the following interface conditions written for all edges $\sigma \in \mathcal{E}_\Gamma$, with $\mathcal{M}_\sigma = \{K, L\}$, $K \in \mathcal{M}^p$, $L \in \mathcal{M}^g$:

$$\begin{cases} \dfrac{1}{\zeta^g} \displaystyle\sum_{\alpha=l,g} V_{K,\sigma}^{\alpha,i}(\mathcal{U}_K^{n,k}, \mathcal{U}_\sigma^{n,k}) \\ \qquad = -\bar{c}_{i,L}^{n,k} |\sigma| (v_{I,\sigma}^{n,k})^+ - c_i^g(\mathcal{U}_\sigma^{n,k}) |\sigma| (v_{I,\sigma}^{n,k})^- - T_\sigma^D (\bar{c}_{i,L}^{n,k} - c_i^g(\mathcal{U}_\sigma^{n,k})), \ i \in \mathcal{C}, \\ p_\sigma^{g,n,k} = p_L^{n,k} + (\mathbf{n} \cdot (\rho^g \mathbf{u} \otimes \mathbf{u} - \mu^g \nabla \mathbf{u}) \mathbf{n})_\sigma^{n,k-1}, \\ \displaystyle\sum_{i \in \mathcal{C}} c_i^\alpha(\mathcal{U}_\sigma^{n,k}) = 1, \ \alpha = g, l, \end{cases} \tag{19}$$

with the gas pressure jump $(\mathbf{n}\cdot(\rho^g\mathbf{u}\otimes\mathbf{u}-\mu^g\nabla\mathbf{u})\mathbf{n})_\sigma^{n,k-1}$ specified in step 2 below.

The coupled system (17-18-19) at each time step n and at each fixed point iteration k is solved using a Newton algorithm. For all cells $K\in\mathcal{M}^p$ and for all edges $\sigma\in\mathcal{E}_\Gamma$ both fugacities f_e and f_a can be eliminated from the non linear system using the closure equations $c_e^\alpha(\mathcal{U})+c_a^\alpha(\mathcal{U})=1$, $\alpha=g,l$ Also, for all $\sigma\in\mathcal{E}_\Gamma$, the normal velocity v_I is eliminated using the equation from (19)

$$v_{I,\sigma}^{n,k}=-\frac{1}{|\sigma|\zeta^g}\sum_{i\in\mathcal{C}}\sum_{\alpha=l,g}V_{K,\sigma}^{\alpha,i}(\mathcal{U}_K^{n,k},\mathcal{U}_\sigma^{n,k}).$$

Using these eliminations, the Jacobian system to be solved at each Newton iteration reduces to Cardinal($\mathcal{C}$) equations and unknowns in each cell $K\in\mathcal{M}^p\cup\mathcal{M}^g$ and at each edge $\sigma\in\mathcal{E}_\Gamma$. This linear system is solved using the sequential version of the SuperLU direct sparse solver [20], [13].

4.1.2 MAC discretization of Step 2

For the MAC discretization of the RANS model (8), it is more convenient to use the following structured mesh notations. The non uniform Cartesian mesh of Ω^g is defined by the set of N_x+1 points along the x axis

$$0=x_{\frac{1}{2}}<\cdots<x_{i-\frac{1}{2}}<x_{i+\frac{1}{2}}<\cdots<x_{N_x+\frac{1}{2}}=L,$$

and by the set of N_y+1 points along the y axis

$$0=y_{\frac{1}{2}}<\cdots<y_{i-\frac{1}{2}}<y_{i+\frac{1}{2}}<\cdots<y_{N_y+\frac{1}{2}}=H_1.$$

Let us define $x_i=\frac{x_{i+\frac{1}{2}}+x_{i-\frac{1}{2}}}{2}$, $i=1,\cdots,N_x$, and $y_j=\frac{y_{j+\frac{1}{2}}+y_{j-\frac{1}{2}}}{2}$, $j=1,\cdots,N_y$.

The discrete unknowns of the staggered MAC discretization are the vertical edge normal velocity perturbations

$$\tilde{u}_{i+\frac{1}{2},j},\ i=0,\cdots,N_x,\ j=1,\cdots,N_y,$$

the horizontal edge normal velocities

$$v_{i,j+\frac{1}{2}}=\tilde{v}_{i,j+\frac{1}{2}},\ i=1,\cdots,N_x,\ j=0,\cdots,N_y,$$

and the cell centered pressure perturbations

$$\tilde{p}_{i,j},\ i=1,\cdots,N_x,\ j=1,\cdots,N_y.$$

The convective fluxes are discretized using a first order upwind approximation of the velocities assuming in our case that $u_t(y_j)+\tilde{u}_{i+\frac{1}{2},j}\geq 0$ and $\tilde{v}_{i,j+\frac{1}{2}}\leq 0$. We refer to [16, 24, 30] for the details of the classical MAC discretization of the system (8) which couples the discrete $\tilde{u}_{i+\frac{1}{2},j}$ momentum conservation equation in the cell $(x_i,x_{i+1})\times(y_{j-\frac{1}{2}},y_{j+\frac{1}{2}})$ for all $i=1,\cdots,N_x-1$, $j=1,\cdots,N_y$, the discrete $\tilde{v}_{i,j+\frac{1}{2}}$ momentum conservation equation in the cell $(x_{i-\frac{1}{2}},x_{i+\frac{1}{2}})\times(y_j,y_{j+1})$ for all $i=1,\cdots,N_x$, $j=1,\cdots,N_y-1$, the discrete divergence free volume conservation equation in the cell $(x_{i-\frac{1}{2}},x_{i+\frac{1}{2}})\times(y_{j-\frac{1}{2}},y_{j+\frac{1}{2}})$ for all $i=1,\cdots,N_x$, $j=1,\cdots,N_y$, and the Dirichlet and outflow boundary conditions for $\tilde{u}$ and $\tilde{v}$.

This discrete system is solved at each time step n and at each fixed point iteration k using a Quasi Newton algorithm where the Jacobian matrix is approximated by dropping the non linear part of the system. The main advantage of this approach is that this approximate Jacobian does not depend on n nor on k. Hence it is factorized only once using a direct sparse linear solver and

a forward-backward sweep is performed at each Quasi Newton iteration. In the above numerical experiments the sequential version of the direct sparse solver SuperLU (see e.g.[13, 20]) is used.

Communications between step 1 and 2: Step 1 sends to step 2 the normal velocities $u^{k,n}_{n,\sigma(i)}$ at the interface where $\sigma(i)$ is the one to one mapping between $i = 1, \cdots, N_x$ and the set of edges $\mathcal{E}_\Gamma$. Step 2 sends to step 1 the normal velocities at the edges $\mathcal{E}^g_{int} \cup \mathcal{E}^g_{out} \cup \mathcal{E}^g_{in}$, as well as the pressure jumps at $\sigma(i)$, $i = 1, \cdots, N_x$ which in practice can be neglected.

In the following numerical experiments the non linear stopping criteria are fixed to

- $\epsilon_{Newton} = 10^{-7}$ for the relative l^2 norm of the residual of the non linear system (17-18-19),
- $\epsilon_{QuasiNewton} = 10^{-6}$ for the relative l^2 norm of the difference between two successive Quasi Newton iterates of the discrete RANS non linear system,
- $\epsilon_{FixedPoint} = 10^{-8}$ on $\|1 - \sum_{i\in\mathcal{C}} c_i\|_{l^\infty}$ for the fixed point iterations of the coupled problem.

4.2 Andra test case with an horizontal gallery

The setting of this test case is exhibited in Figure 2. The porous medium domain $\Omega^p = (0, L) \times (H_1, H_2)$, with $H_1 = 5$ m and $H_2 = 15$ m, includes two rocktypes. The concrete rocktype in the domain $(0, L) \times (H_1, H_1 + 1)$ is defined by the Van-Genuchten parameters $n = 1.54$, $s^l_r = 0.01$, $s^g_r = 0$, $P_r = 2\ 10^6$ Pa, the isotropic permeability $\mathbf{K} = 10^{-18}$ m^2 and the porosity $\phi = 0.3$. The COx rocktype in the domain $(0, L) \times (H_1 + 1, H_2)$ is defined by the Van-Genuchten parameters $n = 1.49$, $s^l_r = 0.4$, $s^g_r = 0$, $P_r = 15\ 10^6$ Pa, the isotropic permeability $\mathbf{K} = 5\ 10^{-20}$ m^2, and the porosity $\phi = 0.15$. The initial and top boundary liquid pressure in the porous medium is set to $p^l_{init} = 40\ 10^5$ Pa, and the temperature is fixed to $T_e = 303$ K both in the porous medium and in the gallery. The initial and input relative humidity in the gallery is fixed to $H_{r,init} = 0.5$ and the ouput and initial pressure in the gallery to $p_{init} = p_{out} = 10^5$ Pa. In the following tests, we evaluate the influence of the input velocity w_{in} and of the length L of the gallery on the mean relative humidity in the gallery and on the mean evaporation rate at the interface. The input velocity w_{in} is set to 0.05, 0.5 or 5 m. s^{-1}, and the length L is set to 25, 100 or 400 m. The simulation is run over a period of 200 years, chosen large enough to reach the stationary state. To assess the numerical convergence of the discrete solutions, a family of Cartesian meshes are tested with increasing sizes set to $Nx \times Ny = 25 \times 50$, 50×100, 100×200, and 200×400. All these meshes are uniform in the x direction and are refined in the direction y on both sides of the interface Γ as well as at the COx and concrete rocktypes interface $y = H_1 + 1$. To fix ideas, the sizes of the first cells at both sides of the interface Γ are set to to δy_1 in the gallery side and to δy_2 in the porous medium side with $(\delta y_1, \delta y_2)$ in meters equal to $(1.62\ 10^{-2}, 6.95\ 10^{-3})$, $(7.09\ 10^{-3}, 3.06\ 10^{-3})$, $(3.32\ 10^{-3}, 1.44\ 10^{-3})$, and $(1.61\ 10^{-3}, 6.96\ 10^{-4})$ for respectively the meshes 25×50, 50×100, 100×200, and 200×400. Note that, with these values of δy_1 on the gallery side, the meshes are refined down to the scale of the laminar boundary layer.

In order to understand the following numerical results, we need to have in mind the orders of magnitude at the interface Γ of the molar fractions which are such that $c^l_a << c^l_e$, $c^g_e << c^g_a$, $c_e << c_a$, and of the molar gas and liquid Darcy fluxes which are such that $|\mathbf{V}^g \cdot \mathbf{n}| << |\mathbf{V}^l \cdot \mathbf{n}|$. It follows that, at the interface Γ, the water component convective flux $\zeta^g c_e \mathbf{u} \cdot \mathbf{n}$ is small compared to the water component diffusive flux $-\zeta^g D^g \nabla c_e \cdot \mathbf{n}$ with a ratio roughly equal to c_e. This can be checked numerically in Figure 3 plotting the mean water component convective and diffusion fluxes at the interface as a function of time. Using this remark, we can explain the shape of the mean evaporation rate at the interface as a function of time exhibited in Figure 5. It classicaly includes

two stages characterized for the first stage by a roughly constant evaporation rate followed for the second stage by a decrease of the evaporation rate down to the stationary state. It is also known that the evaporation rate of the first stage weakly depends on the properties of the porous medium but the duration of the stage does depends on the porous medium properties. This first stage actually corresponds to a value of the water component molar fraction c_e at the interface roughly equal to $\frac{P_{sat}(T_e)}{p_{out}}$ (relative humidity H_r equal to 1) due to a relatively large water influx in the gallery. Using this Dirichlet boundary condition and the previous remark, the value of the water influx can be roughly computed from the solution c_e of the stationary convection diffusion equation in the gallery

$$\left\{\begin{array}{rll} \mathrm{div}\Big(\mathbf{u}_t c_e - (D^g + D_t)\nabla c_e\Big) = 0 & & \text{on } \Omega^g, \\ c_e = \frac{P_{sat}(T_e)}{p_{out}} & & \text{on } \Gamma, \\ c_e = c_{in} & & \text{on } \Gamma^g_{in}, \\ \nabla c_e \cdot \mathbf{n} = 0 & & \text{on } \Gamma^g_{out} \cup \Gamma^g_N. \end{array}\right. \tag{20}$$

which roughly corresponds to the value observed in Figure 5 away from a short transient state. Once the porous medium is sufficiently dried at the interface, the water influx starts to decrease down to a much lower stationary state (case of a top boundary bringing water in the porous medium). This decreasing phase corresponds to the second stage of the drying process. Similarly, as shown in Figure 5, after a rapid transient increase, the relative humidity in the gallery is roughly constant during the first stage with a value which can be computed from the solution c_e of (20). Then, it decreases down to a stationary state during the second stage. These two stages of the simulation and the final stationary state can also be observed in Figure 4 which shows at different times the gas saturation in the porous medium and the water molar fraction in the gallery. Figure 5 exhibits the good convergence in space of the relative humidity in the gallery and of the mean evaporation rate at the interface. Table 1 shows the numerical behavior of the simulations for various choices of the length of the gallery L and of the input velocity w_{in} and for the four meshes. We can observe a good scalability of the Newton and Quasi Newton non linear solvers and a good convergence of the fixed point iterations with roughly two or three fixed point iterations by time step. Finally, Figures 6-8 exhibit the comparison of the relative humidity in the gallery and of the evaporation rate at the interface obtained for the 2D-2D and for the reduced 2D-1D models with various values of the length L and of the input velocity w_{in}. It is clear that the larger the length the better the approximation provided by the reduced model. In all cases, the reduced model provides a good order of magnitude of all quantities of interest. Figure 9 clearly shows that the solutions of the sequential algorithm, obtained with a single fixed point iteration, and of the converged fixed point algorithm can hardly be distinguished.

4.3 Andra test case with a vertical gallery

We consider in this test case a vertical gallery of length $L = 400$ m exhibited in Figure 10. The gallery is now defined by $\Omega^g = (0, H_1) \times (0, L)$ with $H_1 = 5$ m, and the porous medium by $\Omega^p = (H_1, H_2) \times (0, L)$ with $H_2 = 15$ m. The first rocktype for $y \leq 200$ m is defined by the parameters of the COx rocktype of the previous test case. The second rocktype is like the COx rocktype except that the permeability is larger by a factor 100.

The objectives of this test case are the following. Since the duration of the constant evaporation rate stage depends on the permeability, this test case with two different permeabilities along the direction of the gallery should exhibit a non constant evaporation rate even during the first stage of the drying process. Another consequence is that the assumption of a roughly constant water molar fraction along the direction of the gallery which is used to compute the boundary layer thickness of the reduced model should no longer be valid even during the first stage of the drying process. Hence

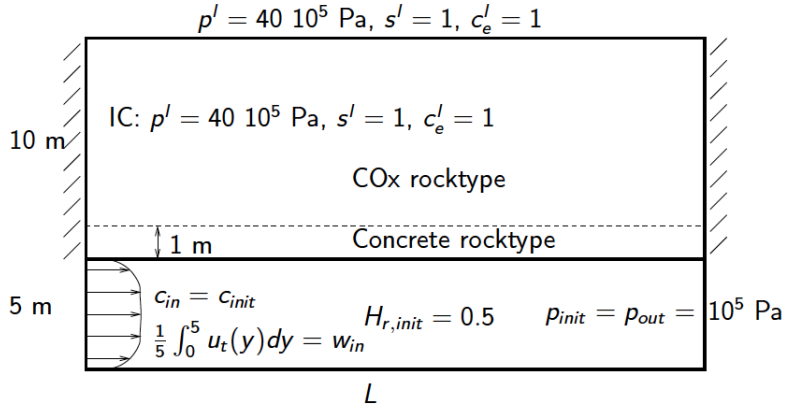

Figure 2: Setting of the Andra test case with an horizontal gallery.

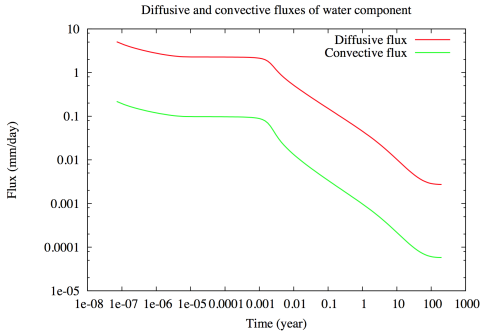

Figure 3: Mean diffusive and convective fluxes of the water component at the interface as a function of time with $L = 100$ m, $w_{in} = 0.5$ m.s^{-1} and the mesh 100×200.

meshes	$N_{\Delta t}$	N_{Chop}	N_{Newton}	N_{Pt}	N_{NVS}	CPU(s)
25×50	123	0	504	239	435	7.56
50×100	123	0	527	257	480	48.64
100×200	123	0	552	277	525	388.47
200×400	123	0	582	287	552	3279.18
meshes	$N_{\Delta t}$	N_{Chop}	N_{Newton}	N_{Pt}	N_{NVS}	CPU(s)
25×50	123	0	591	305	590	8.60
50×100	123	0	636	315	615	58.86
100×200	123	0	690	324	634	486.11
200×400	123	0	753	343	661	4505.81
meshes	$N_{\Delta t}$	N_{Chop}	N_{Newton}	N_{Pt}	N_{NVS}	CPU(s)
25×50	123	0	673	349	694	9.89
50×100	123	0	792	368	726	73.12
100×200	123	0	864	383	778	620.51
200×400	123	0	923	388	786	7262.62

Table 1: For $(L,w_{in}) = (25, 5)$ (above), $(100, 0.5)$ (middle) and $(400, 0.05)$ (below) in m for L and m.s^{-1} for w_{in}, and for each mesh: number $N_{\Delta t}$ of successful time steps, number N_{Chop} of time step chops, number N_{Newton} of Newton iterations, number N_{Pt} of fixed point iterations, number N_{NVS} of quasi-newton iterations, CPU time in seconds.

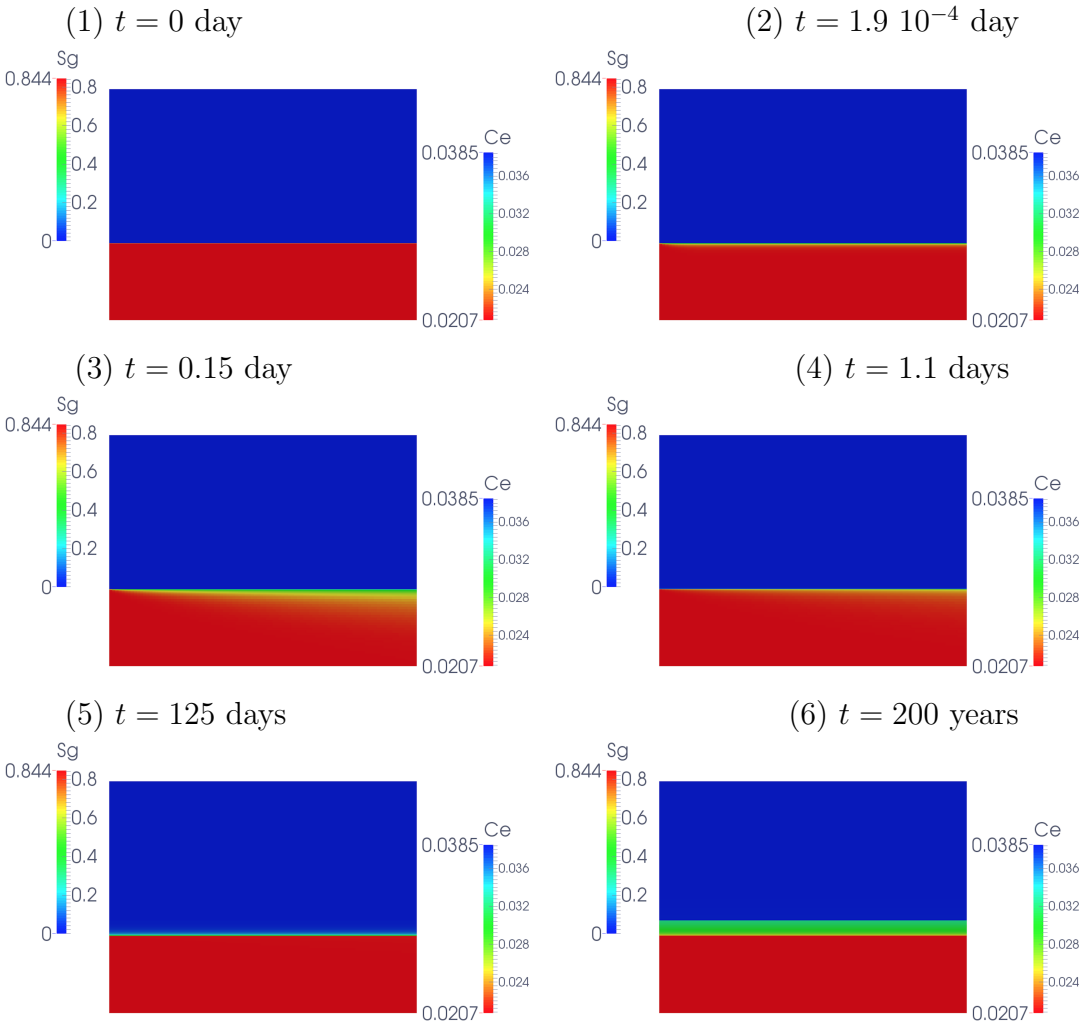

Figure 4: Gas saturation in the porous medium and water molar fraction in the gallery with $L = 100$ m, $w_{in} = 0.5$ m.s^{-1} and the mesh 100×200 at (1) $t = 0$ day, (2) $t = 1.9\ 10^{-4}$ day, (3) $t = 0.15$ day, (4) $t = 1.1$ days, (5) $t = 125$ days, (6) $t = 200$ years.

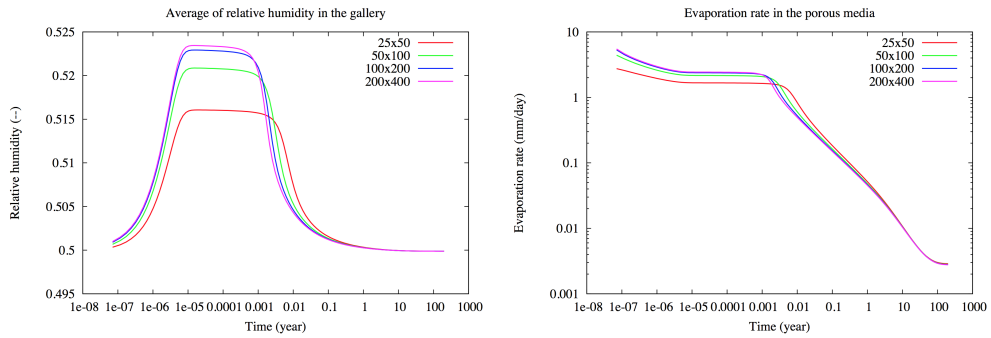

Figure 5: For each mesh and for $L = 100$ m, $w_{in} = 0.5$ m.s^{-1}: average of the relative humidity in the gallery (left) and evaporation rate at the interface (right) as a function of time.

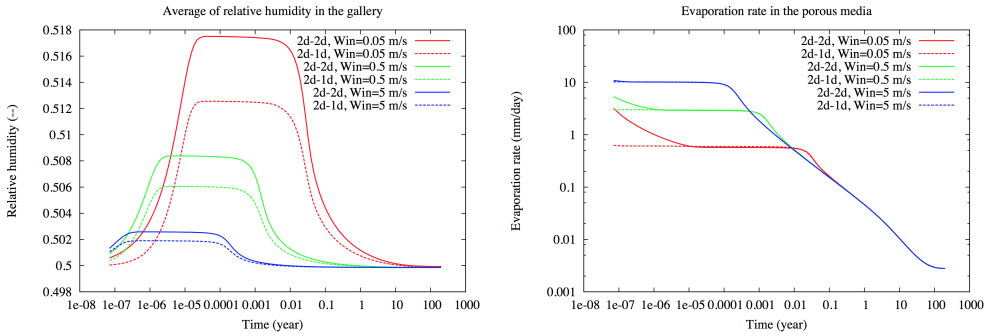

Figure 6: Comparison of the solutions obtained by the 2d-2d and 2d-1d models with $L = 25$ m and the mesh 100×200: average of relative humidity in the gallery (left), evaporation rate at the interface (right) as a function of time.

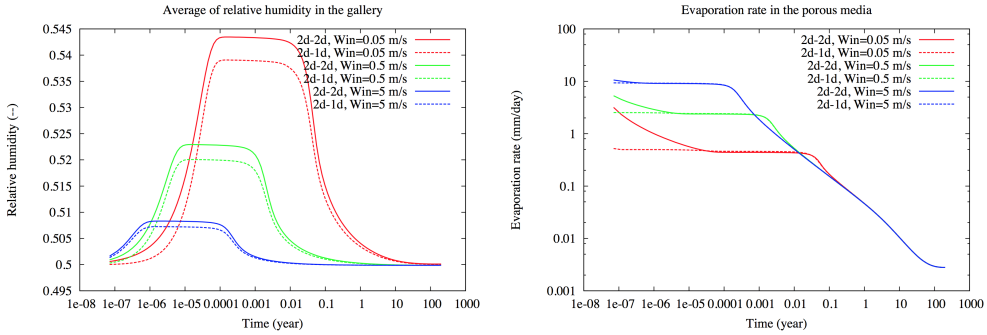

Figure 7: Comparison of the solutions obtained by the 2d-2d and 2d-1d models with $L = 100$ m and the mesh 100×200: average of the relative humidity in the gallery (left), evaporation rate at the interface (right) as a function of time.

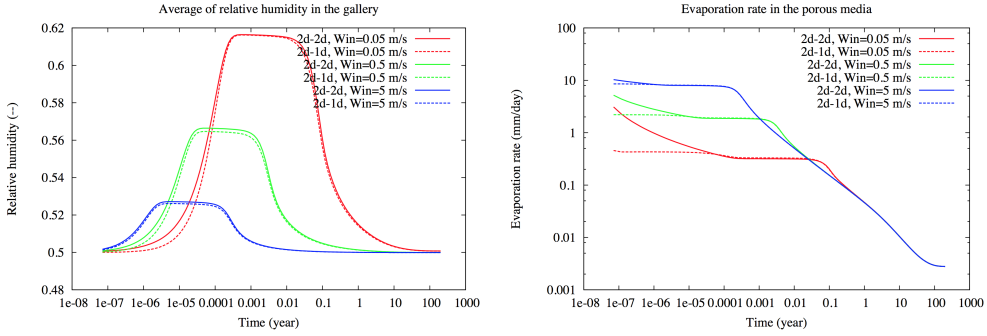

Figure 8: Comparison of the solutions obtained by the 2d-2d and 2d-1d models with $L = 400$ m and the mesh 100×200: average of the relative humidity in the gallery (left), evaporation rate at the interface (right) as a function of time.

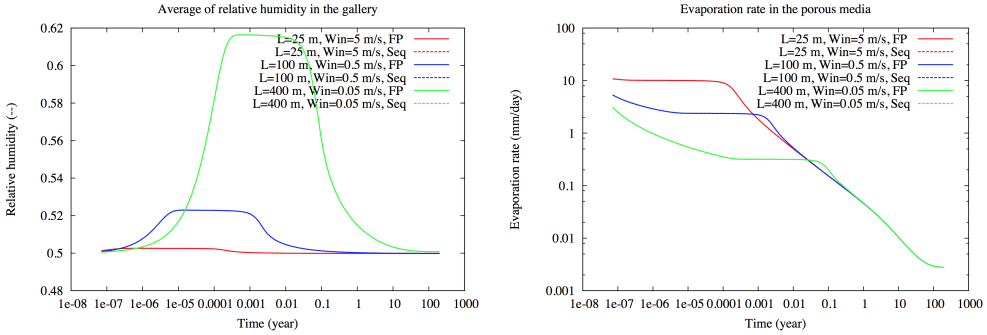

Figure 9: Comparison of the solutions obtained by the fixed-point (FP) and sequential (Seq) algorithms with the mesh 100×200: average of the relative humidity in the gallery (left), evaporation rate at the interface (right) as a function of time.

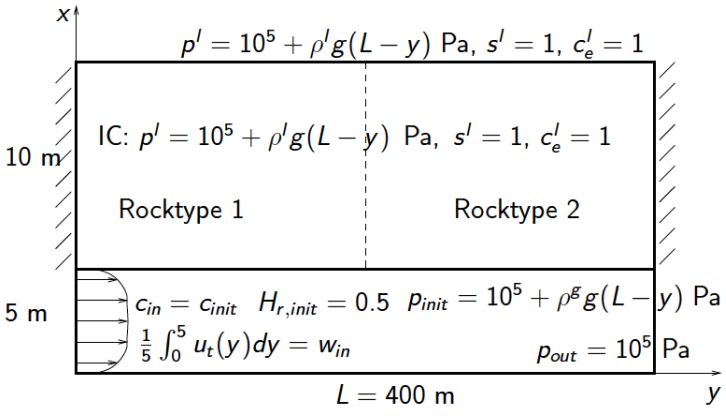

Figure 10: Setting of the Andra test case with a vertical gallery.

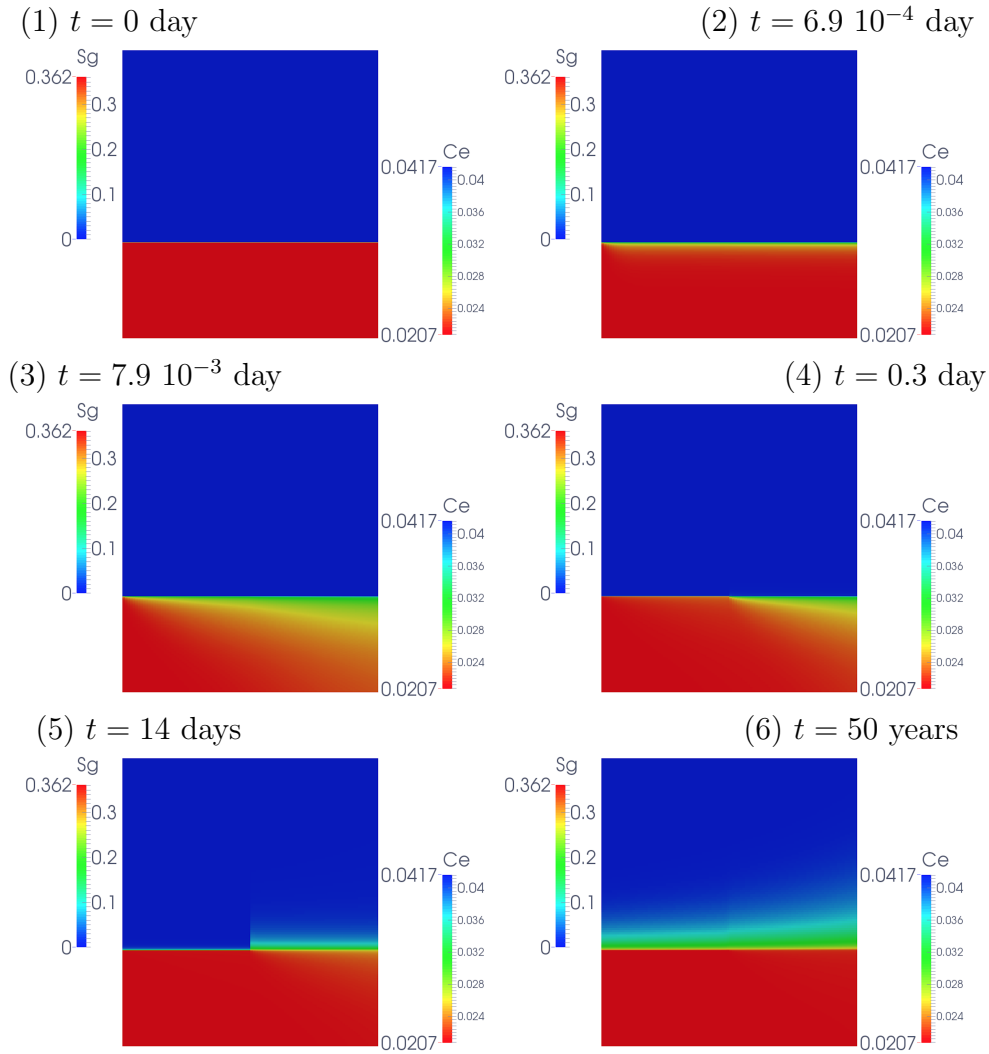

Figure 11: Gas saturation in the porous medium and water molar fraction in the gallery with $w_{in} = 0.5$ m.s^{-1} and the mesh 100×283 at (1) $t = 0$ day, (2) $t = 6.9\ 10^{-4}$ day, (3) $t = 7.9\ 10^{-3}$ day, (4) $t = 0.3$ day, (5) $t = 14$ days, (6) $t = 50$ years.

it is a good test case to challenge the reduced 2D-1D model. The simulation is run over a period of 50 years with an initial time step of 1 s and a maximum time step of 10 years. The numerical solutions are obtained with the meshes $Ny \times Nx = 25 \times 73$, 50×143, 100×283, which are refined on both sides of the interface Γ as in the previous test case.

Figure 12 shows as expected that the evaporation rate and the relative humidity are no longer constant during the first stage of the drying process due to the heterogeneity of the permeability along the gallery. Figure 11 also clearly shows the influence of the two different permeabilities along the gallery on the evaporation rate and on the desaturation of the porous medium. We see that the desaturation front propagates at different time scales in the two rocktype regions. Figure 13 still exhibits a good match between the 2D-2D and the reduced 2D-1D models. However, as expected, it is not as good as in the previous test case. Figure 14 exhibits as previously that the solutions of the sequential and converged fixed point algorithms are basically the same. Table 2 exhibits, as in the previous test case, the good numerical behavior and scalability of the non linear solvers.

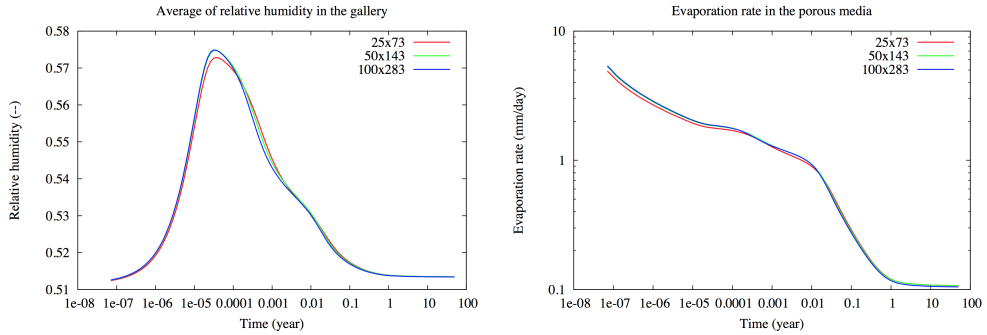

Figure 12: For each mesh and for $w_{in} = 0.5$ m.s^{-1}: average of the relative humidity in the gallery (left) and evaporation rate at the interface (right) as a function of time.

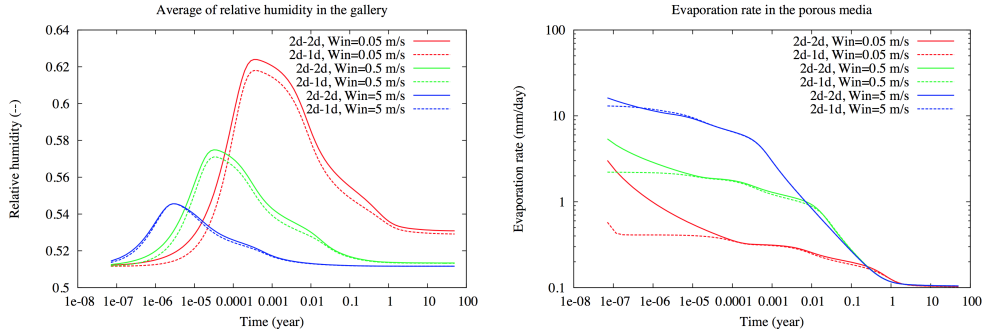

Figure 13: Comparison of the solutions obtained by the 2d-2d and 2d-1d models with the mesh 100×283: average of the relative humidity in the gallery (left), evaporation rate at the interface (right) as a function of time.

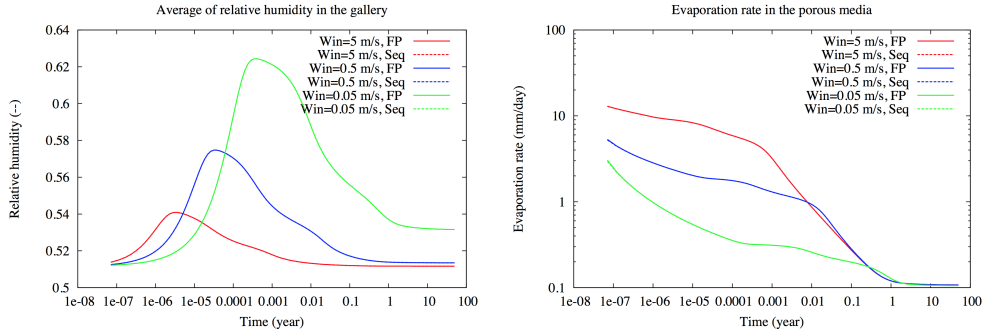

Figure 14: Comparison of the solutions obtained by the fixed-point (FP) and sequential (Seq) algorithms with the mesh 50×143: average of the relative humidity in the gallery (left), evaporation rate at the interface (right) as a function of time.

meshes	$N_{\Delta t}$	N_{Chop}	N_{Newton}	N_{Pt}	N_{NVS}	CPU(s)
25×73	108	0	882	397	765	18.57
50×143	108	0	963	406	805	123.43
100×283	108	0	1054	407	810	1155.48

meshes	$N_{\Delta t}$	N_{Chop}	N_{Newton}	N_{Pt}	N_{NVS}	CPU(s)
25×73	108	0	759	328	619	15.63
50×143	108	0	857	359	662	106.65
100×283	108	0	960	362	685	936.90

meshes	$N_{\Delta t}$	N_{Chop}	N_{Newton}	N_{Pt}	N_{NVS}	CPU(s)
25×73	108	0	595	278	539	12.59
50×143	108	0	648	278	540	85.77
100×283	108	0	706	288	551	760.54

Table 2: For $w_{in} = 0.05$ (above), 0.5 (middle) and 5 (below) in m.s^{-1}, and for each mesh: number $N_{\Delta t}$ of successful time steps, number N_{Chop} of time step chops, number N_{Newton} of Newton iterations, number N_{Pt} of fixed point iterations, number N_{NVS} of quasi-newton iterations, CPU time in seconds.

4.4 Drying test case

In this test case exhibited in Figure 15, we consider the drying by convection of an homogenerous porous medium $\Omega^p = (0, L) \times (H_1, H_2)$ with $L = 1$ m, $H_1 = 0.5$ m, $H_2 = 1.5$ m. The Porous medium is assumed to be closed at the lateral boundaries Γ^p_N and at the top boundary Γ^p_D. The rocktype is defined by the Van-Genuchten parameters $n = 4$, $s^l_r = s^g_r = 0$, $P_r = 15\ 10^3$ Pa, the isotropic permeability $\mathbf{K} = \mathbf{10^{-12}}$ m^2 and the porosity $\phi = 0.15$. The temperature is fixed to a rather high value $T_e = 333$ K in order to increase the liquid evaporation rate. Consequently the water molar fraction at a relative humidity equal to 1 is not so small any more and the water convection flux at the interface is not so negligeable anymore compared with the water diffusive flux. as exhibited in Figure 16. Note also that in this test case, the buoyancy forces in the porous medium are not small any more compared with the capillary forces as it was the case for the horizontal Andra test case. Therefore, the gas which penetrates in the porous medium rises up to the closed top boundary as shown in Figure 17. The simulation is run over a period of 100 days with an initial time step of 10^{-4} s and a maximum time step of 1 day. The numerical solutions are obtained with the meshes $Nx \times Ny = 25 \times 73$, 50×143, 100×283, which are, as for the first test case, refined on both sides of the interface Γ to capture the steep gradient of the liquid pressure on the porous medium side and the laminar boundary layer on the gallery side.

The comparison of the 2D-2D and reduced 2D-1D models exhibited in Figure 19 shows not such a good match for the relative humidity. This is of course due to the fact that the 1D flow assumption in the gallery is of course no longer verified. On the other hand the evaporation rate, the gas velocity and the gas volume still exhibit a very good match. This shows that the approximation provided by the boundary layer thickness model is still good.

Figure 18 shows that the spatial convergence is almost acheived for the coarsest mesh due to the strong refinement at the interface Γ. Figure 20 exhibits as before that the sequential algorithm provides basically the same accuracy than the converged fixed point algorithm. The numerical behavior given by Table 3 is still quite good.

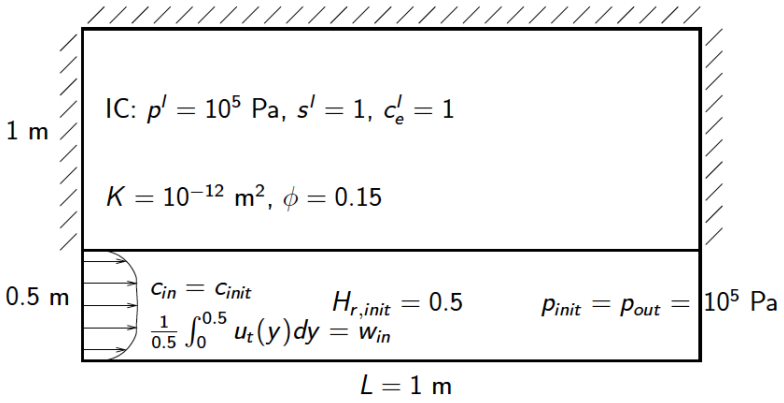

Figure 15: Setting of the drying test case.

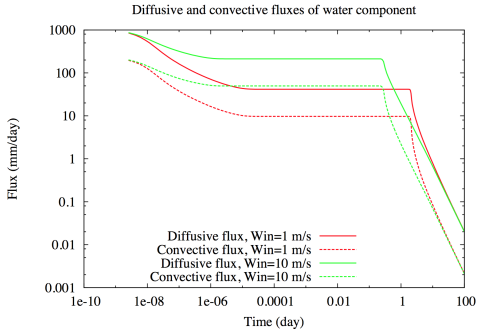

Figure 16: Mean diffusive and convective fluxes of water component at the interface as a function of time with the mesh 100×283.

meshes	$N_{\Delta t}$	N_{Chop}	N_{Newton}	N_{Pt}	N_{NVS}	CPU(s)
25×73	215	2	1879	625	1265	38.00
50×143	218	3	2767	675	1390	334.00
100×283	233	7	4458	752	1562	4251.28
meshes	$N_{\Delta t}$	N_{Chop}	N_{Newton}	N_{Pt}	N_{NVS}	CPU(s)
25×73	208	0	1446	551	1017	30.47
50×143	212	1	2233	593	1104	271.19
100×283	223	4	3561	643	1183	3485.42

Table 3: For $w_{in} = 1$ (above) and 10 (below) in m.s^{-1} , and for each mesh: number $N_{\Delta t}$ of successful time steps, number N_{Chop} of time step chops, number N_{Newton} of Newton iterations, number N_{Pt} of fixed point iterations, number N_{NVS} of quasi-newton iterations, CPU time in seconds.

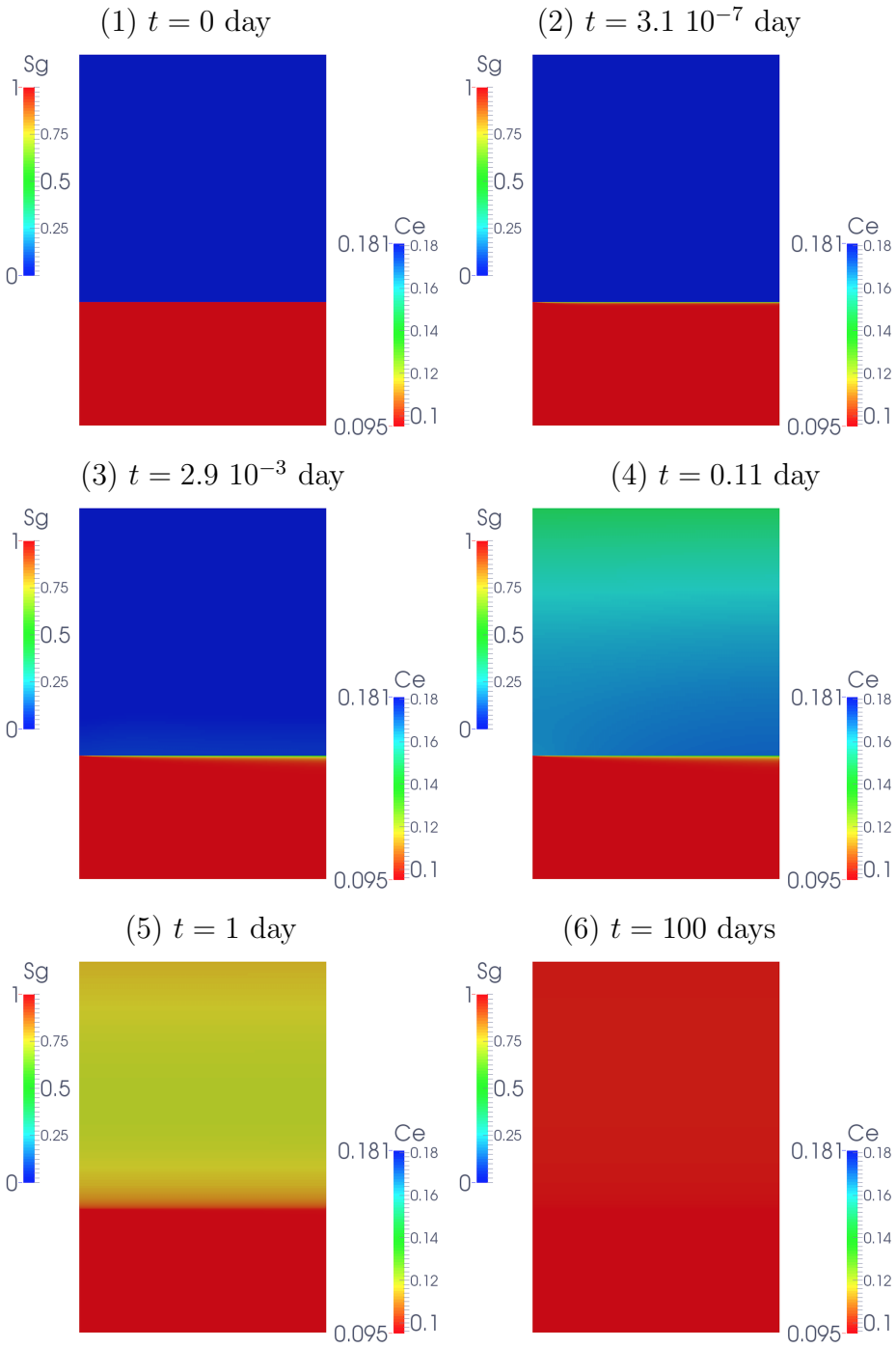

Figure 17: Gas saturation in the porous medium and water molar fraction in the gallery with $w_{in} = 10$ m.s^{-1} and the mesh 100×283 at (1) $t = 0$ day, (2) $t = 3.1\ 10^{-7}$ day, (3) $t = 2.9\ 10^{-3}$ day, (4) $t = 0.11$ day, (5) $t = 1$ day, (6) $t = 100$ days.

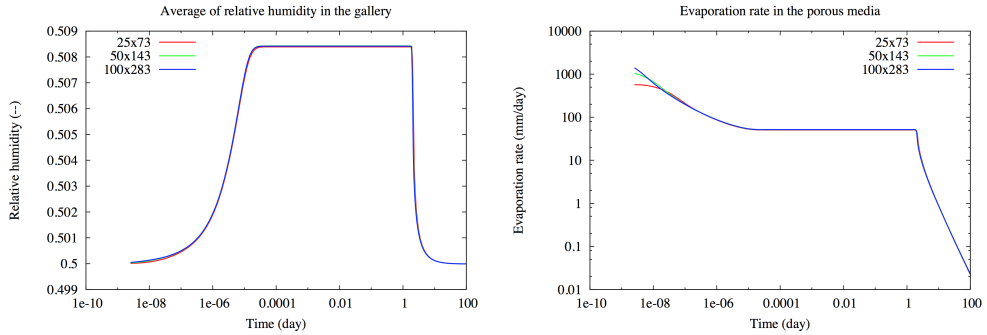

Figure 18: For each mesh and for $w_{in} = 1$ m.s^{-1}: average of the relative humidity in the gallery (left) and evaporation rate at the interface (right) as a function of time.

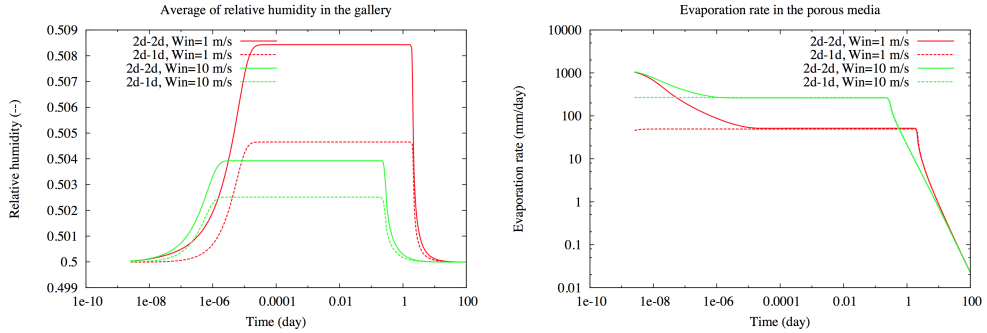

Figure 19: Comparison of the solutions obtained by the 2d-2d and 2d-1d models with the mesh 50×143: average of the relative humidity in the gallery (left), evaporation rate at the interface (right) as a function of time.

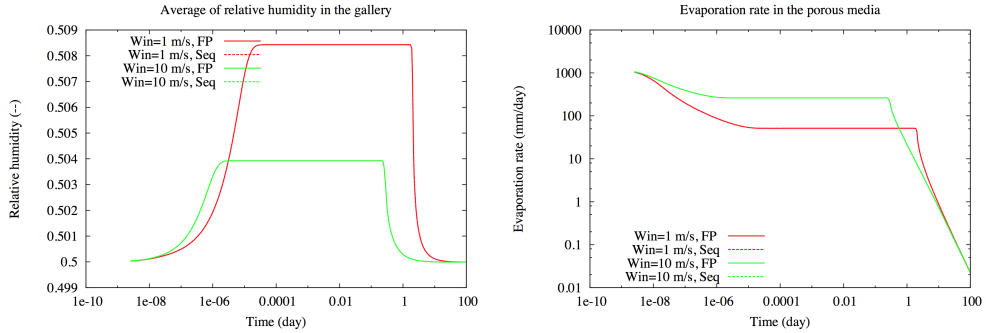

Figure 20: Comparison of the solutions obtained by the fixed-point (FP) and sequential (Seq) algorithms with the mesh 50×143: average of the relative humidity in the gallery (left), evaporation rate at the interface (right) as a function of time.

5 Conclusions

In this article, a splitting algorithm has been introduced to solve the problem coupling the liquid gas Darcy flow in the porous medium and the free gas flow in the gallery. It can be used either as a fixed point or sequential algorithm. Our splitting is chosen in order to preserve the strong coupling between the water molar fraction in the free flow domain and the liquid pressure and liquid flux at the interface, while it relaxes the weak coupling between the porous medium and the velocity and pressure in the free flow domain. A good convergence of this fixed point algorithm has been observed on Andra and drying test cases in a simple 2D geometrical setting. This algorithm has the advantage compared with fully coupled approaches [3, 17, 22] to lead to the non linear solutions of simpler sub-systems. It also allows large time steps at the time scale of the porous medium as opposed to sequential algorithms [12, 10] for which the time steps are limited by the time scale of the free gas flow.

This model is compared with a reduced model using a 1D model in the free flow domain. This reduced model uses an approximation of the gas molar fraction boundary layer thickness based on a low frequency approximation of a Steklov Poincaré operator. The comparisons performed on the 2D test cases show a very good match of the evaporation rate. It also exhibits a good match of the relative humidity in the gallery especially, as expected, for high ratios between the length and the diameter of the gallery.

References

[1] Angelini, O., Chavant, C., Chénier, E., Eymard, R. and Granet, S., *Finite volume approximation of a diffusion-dissolution model and application to nuclear waste storage*, Mathematics and Computers in Simulation, **81(10)**, pp. 2001-2017, 2011.

[2] Aziz, K. and Settari, A., *Petroleum Reservoir Simulation*, Applied Science Publishers, 1979.

[3] Baber, K., Mosthaf, K., Flemisch, B., Helmig, R. and Müthing, S., *Numerical scheme for coupling two-phase compositional porous-media flow and one-phase compositional free flow*. IMA Journal of Applied Mathematics, **77(6)**, 2012.

[4] Beavers, G. S. and Joseph, D. D. Boundary conditions at a naturally permeable wall. Journal of Fluid Mechanics, 30:197-207, 1967.

[5] Bird, R. B., Stewart, W. E., and Lightfoot, E. N. Transport phenomena. John Wiley and Sons, 2007.

[6] Brenner, K., Masson, R., Trenty, L. and Zhang, Y., *Coupling of a two phase gas liquid compositional 3D Darcy flow with a 1D compositional free gas flow*, ESAIM, M2AN, accepted november 2015, http://dx.doi.org/10.1051/m2an/2015091.

[7] Chassaing, P., Turbulence en Mécanique des Fluides, analyse du phénomène en vue de sa modélisation à l'usage de l'ingénieur, Cépaduès- Editions, 2000.

[8] Coats, K. H., *An equation of state compositional model*, SPE Reservoir Simulation Symposium Journal, pp. 363-376, 1980.

[9] Coats, K. H., *Implicit compositional simulation of single-porosity and dual-porosity reservoirs*, SPE Symposium on Reservoir Simulation, 1989.

[10] Defraeye, T., *Convective heat and mass transfer at exterior building surfaces*, PhD thesis, Catholic University of Leuven, Leuven, Belgium, 2011.

[11] Defraeye, T., *Advanced computational modelling of drying processes, a review*, Applied Energy, **131**, pp. 323-344, 2014.

[12] Defraeye, T., Blocken, B. and Carmeliet, J., *Analysis of convective heat and mass transfer coefficients for convective dring of a porous flat plate by conjugate modelling*, Int. J. of Heat and Mass Transfer, **55**, pp. 112-124, 2012.

[13] Demmel, J. W., Eisenstat, S. C., Gilbert, J. R., Li, X. S., and Liu, J. W. H., *A supernodal approach to sparse partial pivoting, SIAM J. Matrix Analysis and Applications*, **20(3)**, pp. 720-755, 1999.

[14] Discacciati, M., Miglio, E. and Quarteroni, A., *Mathematical and numerical models for coupling surface and groundwater flows*, Appl. Num. Math., **43**, 2002.

[15] Girault, V. and Rivière, B., *DG approximation of coupled Navier-Stokes and Darcy equations by beaver-joseph-saffman interface condition*, SIAM J. Numer. Anal., **47**, 2009.

[16] Harlow F. and Welch, J., *Numerical calculation of time-dependent viscous incompressible flow of fluid with a free surface*, Physics of Fluids, **8**, pp. 2182-2189, 1965.

[17] Helmig, R., Flemisch, B., Wolff, M., Ebigbo, A. and Class, H., *Model coupling for multiphase flow in porous media*, Advances in Water Resources, **51**, 2013.

[18] Japhet, C., Nataf, F. and Rogier, F., *The Optimized Order 2 Method. Application to Convection-Diffusion Problems*, Future generation computer systems, **18(1)**, 17-30, 2001

[19] Lauser, A., Hager, C., Helmig, R. and Wohlmuth, B., *A new approach for phase transitions in miscible multi-phase flow in porous media*, Advances in Water Resources, **34**, pp. 957-966, 2011.

[20] Li, X. S., Demmel, J. W., Gilbert, J. R., Grigori, L., Shao, M. and Yamazaki, I., Technical report LBNL-44289, Lawrence Berkeley National Laboratory, SuperLU Users' Guide, September 1999, http://crd.lbl.gov/ xiaoye/SuperLU.

[21] Masson, R., Trenty, L. and Zhang, Y., *Formulation of two phase gas liquid compositional Darcy flows with phase transitions*, International Journal of Finite Volume, **11**, 2014.

[22] Mosthaf, K., *Modeling and Analysis of Coupled Porous-Medium and Free Flow with Application to Evaporation Processes*, PhD Thesis, University of Stuttgart, 2013

[23] Mosthaf, K., Baber, K., Flemisch, B., Helmig, R., Leijnse, A., Rybak, I. and Wohlmuth, B., *A coupling concept for two-phase compositional porous-medium and single-phase compositional free flow*, Water Resources Research, **47(10)**, 2011

[24] Patankar, S., *Numerical heat transfer and fluid flow. Series in Computational Methods in Mechanics and Thermal Sciences*, **XIII**. Washington - New York - London: Hemisphere Publishing Corporation; New York. McGraw-Hill Book Company, 1980.

[25] Peaceman, D. W., *Fundamentals of Numerical Reservoir Simulations*, Elsevier, 1977.

[26] Saad, Y., *Iterative Methods for Sparse Linear Systems*, 2nd edition, SIAM, Philadelphia, PA, 2003

[27] Saad, Y., http://www-users.cs.umn.edu/ saad/software/

[28] Thual, O., Hydrodynamique de l'environnement, éditions de l'Ecole polytechnique, 2010.

[29] Tran, Q. H., Ferre, D., C. Pauchon, C. and Masella, J. P., *Transient Simulation of Two-Phase Flows in Pipes*, Oil & Gas Science and Technology, **53(6)**, pp. 801-811, 1998.

[30] Wesseling. P., *Principles of Computational Fluid Dynamics*, Springer, 2001.